

Three-dimensional morphometric analysis reveals time-dependent structural changes in microglia and astrocytes in the central amygdala and hypothalamic paraventricular nucleus of heart failure rats

Ferdinand Althammer

Georgia State University

Hildebrando Candido Ferreira-Neto

Georgia State University

Myurajan Rubaharan

Georgia State University

Ranjan Kumer Roy

Georgia State University

Javier E Stern (✉ jstern@gsu.edu)

Georgia State University

Research

Keywords: hypothalamus, amygdala, microglia, astrocytes, A1, behavior, cytokines, heart failure, neuroinflammation, autonomic

Posted Date: January 28th, 2020

DOI: <https://doi.org/10.21203/rs.2.22086/v1>

License:  This work is licensed under a Creative Commons Attribution 4.0 International License.

[Read Full License](#)

Abstract

Background

Cardiovascular diseases, including heart failure are the most common cause of death globally. Recent studies support a high degree of comorbidity between heart failure and cognitive and mood disorders resulting in memory loss, depression and anxiety. While neuroinflammation in the hypothalamic paraventricular nucleus has been shown to contribute to autonomic/cardiovascular dysregulation in heart failure, mechanisms underlying cognitive and mood disorders in this disease remain elusive. The goal of this study was to quantitatively assess several markers of neuroinflammation in the central amygdala, a critical forebrain region involved in emotion and cognition, and to compare the time course of neuroinflammation between the central amygdala and paraventricular nucleus during the progression of heart failure.

Methods

We developed and implemented a comprehensive microglial/astrocyte profiler for precise three-dimensional morphometric analysis of individual microglia and astrocytes in specific brain nuclei at different time points during the progression of heart failure. To this end, we used a well-established ischemic heart failure rat model. Morphometric studies were complemented with quantification of various proinflammatory cytokines and A1/A2 astrocyte markers via qPCR.

Results

We report a drastic structural remodeling of central amygdala microglia and astrocytes during heart failure that affected cell volume, surface area, filament length, dendritic branches, resulting overall in somatic swelling and deramification, indicative of an activated microglial state. These changes occurred in a time-dependent manner and were delayed compared to changes in the hypothalamic paraventricular nucleus. Morphometric changes correlated with elevated mRNA levels of proinflammatory cytokines and markers of reactive neurotoxic astrocytes in the paraventricular nucleus and central amygdala during heart failure.

Conclusion

We provide evidence that in addition to the previously described hypothalamic neuroinflammation implicated in sympathohumoral activation during heart failure, microglia and astrocytes within the central amygdala also undergo structural remodeling indicative of glial shifts towards an activated and neurotoxic phenotype, respectively. Thus, our studies suggest that neuroinflammation in the amygdala stands as a novel pathophysiological mechanism and therapeutic target for alleviating comorbid emotional and cognitive deficits commonly observed at later stages during the course of heart failure.

Background

Cardiovascular diseases (CVDs) are the major cause of death globally, with 17.9 million people dying from CVDs in 2016, thereby representing 31% of all global deaths (World Health Organization, 2017). The vast majority of CVD-related deaths (85%) can be attributed to stroke and heart failure (HF) with their accompanying detrimental effects on the human body, albeit there might be substantial geographic differences in survivability rates (1). A growing body of clinical studies suggests a high degree of comorbidity between CVDs and cognitive impairments and emotional distress (2-4). In fact, 20-40% of all HF patients develop major depression and display anxiety levels significantly higher than the healthy population (2, 3, 5, 6), which usually appear later than the cardiovascular and autonomic-related symptoms (7). However, the precise underlying neuronal substrates and mechanisms leading to mood disorders and cognitive impairments after HF remain largely unknown. Using the rodent left coronary ligation HF model, studies demonstrated that HF mice and rats exhibited behavioral changes including increased anxiety, depression, social impairments and anhedonia (8-10).

The paraventricular nucleus of the hypothalamus (PVN) is a key structure for the regulation of sympathetic outflow and cardiovascular control (11-14), playing thus a major role in bodily homeostasis and neuroendocrine control (15-17). These actions are mediated via direct innervation of sympathetic-related brainstem and spinal cord neurons (11-14). There is also compelling evidence supporting a critical role for the PVN in the onset and maintenance of sympathohumoral activation during HF (18-22). Importantly, neuroinflammation (NI) within the PVN has been described as a hallmark pathophysiological mechanism contributing to increased sympathetic outflow during this disease (23-26). The PVN is also recognized as an important center in emotional regulation and harbors a variety of cells producing different neuropeptides (27-29). In line with this, the PVN directly communicates with the lateral subdivision (CeL) of the Central Amygdala (CeA), which plays an important role in depression (30, 31), fear and anxiety (32-34). Oxytocin(OT)-synthesizing neurons in the PVN project long-range axonal terminals to the CeL, where the local release of OT directly regulates anxiety levels (35, 36), fear memories and fear extinction (37, 38). Moreover, a recent study highlighted the pivotal role of OT signaling in the CeA in mouse models of depression (39). While NI in HF rats has been previously described (25, 26), very little is known about HF-induced NI in other brain areas, such as the CeA, and the respective temporal relation to the onset of NI in the PVN.

NI is predominantly mediated by microglia, the immune cells that take up residence in the brain parenchyma (40, 41). While classical markers such as increased microglial density, increased expression of ionized calcium-binding adapter molecule 1 (IBA1) and various cytokines are widely used to assess NI, they fall short of addressing detailed microglial morphology changes during this pathological process. This is critical because diverse microglial morphometric features are not only associated to diverse microglial functions (42, 43), but more importantly, they have been recently associated to different stages in the spatio-temporal progression of the NI process (44). In this sense, classical two-dimensional maximum projection analysis cannot be used to assess microglial cellular or somatic volume. In light of these recent findings, it becomes clear that detailed 3D analysis of microglia cell morphology is of paramount importance, especially considering microglial heterogeneity and brain region-specific differences in size, density or activation stages (45). Such detailed analysis and quantification of

microglial morphometry in the PVN and CeA under control and disease conditions, such as HF has, to the best of our knowledge, not been performed yet. Given that NI involves an intricate interplay between microglia and astrocytes (46-48), we were also interested to determine whether HF would alter astrocyte function and morphology as well.

To this end, we created a comprehensive glial morphometric profiler and used a novel approach to perform a detailed quantitative analysis of microglial and astrocyte morphology in the PVN and CeA of HF rats in a time-dependent manner 8, 14 and 16 weeks (abbreviated as 8w, 14w and 16w) after the onset of the disease. Moreover, we correlated these morphological parameters with the assessment of various classical markers for NI via qPCR (IBA1, GFAP, TNF- α , IL-1 β and IL-6) as well as markers for astrocyte A1 (neurotoxic) and A2 neuroprotective phenotypes (Serp1, C3, Sphk1 and Tm4sf1) (48-51). Our results highlight for the first time that in addition to the PVN, HF also induces a robust microglial/astrocyte cell remodeling and activation as well as increased cytokine levels in the CeA, a critical forebrain region involved in emotion and cognition. NI-related changes in the CeA occurred with a delayed time course compared to those in the PVN, and could potentially contribute to cognitive impairment and mood disorders observed at later stages of the disease in HF patients.

Materials And Methods

All performed experiments were approved by the Georgia State University Institutional Animal Care and Use Committee (IACUC) and carried out in agreement with the IACUC guidelines. At all time, animals had *ad libitum* access to food and water and all efforts were made to minimize suffering and the numbers of animals used for this study.

Animals

We used male Wistar rats (5 weeks old at surgery, 180-200g, Envigo) for all experiments (total n=44, immunohistochemistry and IMARIS analysis: 28; qPCR: 18). Rats were housed in cages (2 per cage) under constant temperature ($22 \pm 2^\circ\text{C}$) and humidity ($55 \pm 5\%$) on a 12-h light cycle (lights on: 08:00-20:00).

Heart failure surgery and Echocardiography

HF was induced by coronary artery ligation as previously described (21). In brief, animals were anaesthetized using 4% isoflurane and intubated for mechanical ventilation. To exteriorize the heart, we performed a left thoracotomy. The ligation was performed on the main diagonal branch of the left anterior descending coronary artery. Animals received buprenorphine SR-LAB (0.5 mg/kg, S.C.; ZooPharm, Windsor, CO, USA) before the surgical procedure to minimize postsurgical pain. Sham animals underwent the same procedure except the occlusion of the left coronary artery. Five weeks after the surgery we performed transthoracic echocardiography (Vevo 3100 systems; Visual Sonics, Toronto, ON; Canada) under light isoflurane (2-3%) anesthesia. We obtained the left ventricle internal diameter and the left diameter of the ventricle posterior and anterior walls in the short-axis motion imaging mode to calculate

the ejection fraction (EF). Animals with an EF <50% were considered as HF. The average EFs were $79.13 \pm 1.57\%$ (sham, n=21) and $32.48 \pm 2.01\%$ (HF, n=21). Animals were used 8, 14 or 16 weeks after the HF surgery and allocated to the respective groups as indicated in the individual experiments. In addition, we used an additional naive control group, which comprised rats that did not undergo any surgical procedure.

Immunohistochemistry

Following pentobarbital-induced anesthesia (Euthasol, Virbac, ANADA #200-071, Fort Worth, TX, USA, 0.5 mL, i.p.), rats were first perfused at a speed of 20mL/min with 0.01M PBS (200mL, 4°C) through the left ventricle followed by 4% PFA (in 0.3M PBS, 200mL, 4°C), while the right atrium was opened with an incision. Brains were post-fixed for 24 hours in 4% PFA at 4°C and transferred into a 30% sucrose solution (in 0.01M PBS) at 4°C for 3-4 days. For immunohistochemistry, 40 μ m slices were cut using a Leica Cryostat (CM3050 S) and brain slices were kept in 0.01M PBS at 4°C until used for staining. Brain slices containing the PVN (A/P, Bregma: -1.1mm to -1.6mm) and the CeA (A/P, Bregma: -2.0 mm to -2.8 mm) were blocked with 5% Normal Horse Serum in 0.01M PBS for 1h at room temperature. To identify the PVN and CeA topographically, we used the supraoptic nucleus and fornix, as well as the optic tract and commissural stria terminalis as landmarks, respectively. After a 15-min washing in 0.01M PBS, brain slices were incubated for 24h in 0.01M PBS, 0.1% Triton-X, 0.04% NaN₃ containing 1:1000 of anti-IBA1 (polyclonal rabbit, Wako, 019-19741, Lot: CAK1997), 1:1000 anti-glutamine synthetase (monoclonal mouse, Merck Milipore, MAB 302, clone GS-6) or anti-GFAP (goat polyclonal, abcam, ab53554) at room temperature. Following 15-min washing in 0.01M PBS, sections were incubated in 0.01M PBS, 0.1% Triton-X, 0.04% NaN₃ with 1:500 Alexa Fluor 488/594-conjugated donkey anti-rabbit/goat/mouse (Jackson ImmunoResearch, 711-585-152, 705-585-147, 715-545-151) for 4 hours at RT. Brain slices were washed again for 15 mins in 0.01M PBS and mounted using antifade mounting medium (Vectashield H-1500).

Confocal microscopy and 3D IMARIS analysis

For the 3D reconstruction of microglia, we took Z-stack images (50 μ m depth, 1 μ m steps, 40x magnification) of PVN, CeA (lateral and medial subdivision of the CeA, but not the capsular subdivision) and somatosensory cortex 1 barrel field (S1BF) using a Zeiss LSM 780 confocal microscope (1024x1024 pixel, 16-bit depth, pixel size 0.63-micron, zoom 0.7). Raw czi files were used for further analysis using IMARIS software (Version 9.31, Oxford Instruments). First, IMARIS was used to reconstruct the microglial surface using the following custom settings: surfaces Detail 0.700 μ m (smooth); thresholding Background subtraction (Local Contrast), diameter of largest Sphere, which fits into the object: 2.00; Color: base, diffusion transparency: 65%. After surface reconstruction, we used the filter function to remove unspecific background signals: Filter: Volume max – 400 μ m³. All microglia with incomplete somata (cut by either the x, y or z plane) were manually removed and not included in further analysis. In addition, reconstructed entities that were clearly not microglia (i.e. filaments without soma) were also manually removed. Fused microglia that were falsely recognized as one entity by the software were

manually separated using the cut function, or entirely removed from the sample if a separation was not feasible. The 'filter/area function' was used to remove small microglial segments that occurred during manual. After deletion of all background signals the 'mask all' function was used to create the final surface reconstruction. Next, the surface reconstruction was used as the template for the filament reconstruction using the following custom settings: detect new starting points: largest Diameter 7.00 μm , seed points 0.300 μm ; remove seed points around starting points: diameter of sphere regions: 15 μm . Seed points were corrected for (either placed in or removed from the center of the somata) manually if the IMARIS algorithm placed them incorrectly. All surface and filament parameters were exported into separate Excel files and used for data analysis. For all quantifications, we used 6-8 40x z-stacks per animal (2 z-stacks per brain hemisphere). On average, the reconstruction of a single z-stack took 15 minutes using a computer suited for IMARIS analysis (Intel Core i7 8700 @3.2 GHz, 64 GB RAM, x-64-bit, Windows 10 Enterprise), which included the manual removal of microglia. All images used for analysis were taken with the same confocal settings (pinhole, laser intensity, digital gain and digital offset).

Sholl analysis

Sholl analysis was performed using IMARIS in the filament reconstruction mode and individual data sets were exported into separate Excel files for further analysis. We defined a threshold for microglial activation (peak number for Sholl intersections per microglia): <10.0. Intersections (high activity), >9.9 (low activity) and we calculated microglial activation based on these defined thresholds. For the total number of Sholl intersections we added together all the intersections (from each individual sphere) per individual microglia.

2D thresholding analysis of z-stack projections using FIJI

Conventional IBA1 and GFAP immunoreactivity intensity and density analysis of two-dimensional maximum projections was performed using FIJI. First, we set thresholds for individual 16-bit images using the 'Image/Adjust/Threshold' function (ranging from 65-110). Next, we used the 'Analyze/Measure' function with prior specification of 'Limit to Threshold' (intensity, ranging from 108 to 154 AU) or 'Area fraction' (density, ranging from 14.0% to 21.5%) under 'Analyze/Set Measurements'. All images used for analysis were taken with the same confocal settings (pinhole, laser intensity, digital gain and digital offset)

Reverse transcription polymerase chain reaction (RT-PCR) and quantitative real time PCR (qPCR)

RNA extraction and isolation were performed using the miRNAeasy Mini kit (Qiagen, Cat. No. 217004) and the QIAzol Lysis Reagent (Qiagen, Mat. No. 1023537). Briefly, 250 μm -thick tissue sections were made in cryostat (-20°C, Leica, CM3050S) and punches from the PVN (2 mm punches, 4 punches per animal), CeA (1 mm punches, 8 punches per animal) and prelimbic cortex (PLC, 2 mm punches, 4 punches per animal) were collected and kept in dry ice until the RNA extraction procedure. RNA concentration was measured using NanoDrop One (Thermo Scientific). cDNA synthesis was performed using the iScriptTM gDNA Clear cDNA Synthesis Kit (BIO RAD, cat. no. 1725035) and the SimpliAmp

Thermal Cycler (applied biosystems, Thermo Fisher Scientific) following the manufacturer's protocol. qPCR was conducted using the following 10x QuantiTect primers (diluted in 1.1 mL TE ph 8.0) purchased from Qiagen: IBA1 (QT01591751), GFAP, IL-1b (QT00181657), IL-6 (QT00182896), Serping1 (QT01607326), C3 (QT00187159), Tm4sf1 (QT01588034), Sphk1 (QT00182035), TNF-a (QT00182896) and b-Actin (QT00193473, used as the reference gene). All individual qPCR reactions (brain region, primer and condition) were triplicated.

Statistical analysis

All statistical analyses were performed using GraphPad Prism 8 (GraphPad Software, California, USA). The significance of differences was determined using Student's t test or two-way ANOVA for two-group comparisons followed by Tukey post-hoc test, as indicated throughout the text. Results are expressed as mean \pm standard error of the mean (SEM). If not mentioned otherwise, statistical comparisons were performed between HF groups and their respective sham groups. Results were considered statistically significant if $p < 0.05$ and are presented as * for $p < 0.05$, ** for $p < 0.01$ and *** for $p < 0.0001$ in the respective Figures.

Results

Development and validation of a comprehensive microglia profiler to obtain an in-depth 3D morphometric analysis of various cellular parameters

Classic assessment of NI relies on the measurement of cytokine levels, as well as 2D-morphological analysis, which only provides very limited information about IBA1 immunoreactivity intensity and cellular density. Since microglia operate in a three-dimensional space it becomes clear that important information about intricate microglial cell remodeling gets lost, because of the dimensional restriction imposed by 2D imaging. In fact, when we performed a conventional 2D analysis of IBA immunoreactivity we found no significant differences in microglial density between sham and HF rats in both the PVN (40x z-stack, sham 14w: 29.1 ± 3 cells vs HF 14w: 30.4 ± 3 cells, n.s., n=4) and the CeA (40x z-stack, sham 14w: 28.6 ± 3 cells vs. HF 14w: 29.5 ± 2 cells, n.s., n=4) (Fig. 1c, d).

We then used a novel approach we developed using IMARIS to perform 3D reconstruction of microglia and astrocytes, allowing us to assess surface area, cell volume, filament length, dendritic branches and morphometric complexity (Fig. 2a). In brief, we took 50 μ m z-stack confocal images (16-bit, 1 μ m steps, 40x objective) of brain slices stained with IBA1 and exported czi files for further analysis in IMARIS. The raw image was used to reconstruct surface and filaments of individually recognized microglia cells (Fig. 2b). Incompletely stained microglia were not included into our analysis (detailed description of IMARIS-based analysis can be found in 'Material and Methods'). This method allows an unbiased high throughput analysis of various cellular features and is a universally applicable tool for morphometric analysis of different cell types under various conditions. To assess whether the sham surgery itself resulted in microglia morphometric alterations over time, we perfused naïve (20 weeks old, n=2) and sham rats (8-, 14- and 16-weeks post-surgery, n=4/group). We stained brain sections containing the PVN

and the CeA with IBA1 and analyzed microglial profiles using IMARIS. We did not observe any significant changes in the PVN or CeA of sham rats in any of these parameters either when compared to naive rats (20w), or as a function of time after the surgical procedure (8w, 14w or 16w, Fig. 3a-d). Therefore, we decided to pool together the three sham groups for further analysis.

HF-induced a time-dependent NI and morphometric microglial changes in the PVN that are already evident at 8 weeks post-surgery

To study potential HF-induced inflammatory responses in the PVN and CeA over time, we perfused sham and HF rats at 8, 14 and 16 weeks after the surgery (n=4/group) and assessed microglial surface area, cell volume, filament length, dendritic branches, dendritic segments, filament terminals and IBA1 density. Representative confocal images of PVN microglia of sham and HF rats 16-weeks post-surgery are shown in Fig. 4a. As depicted in Fig. 4b and c, we found significant morphometric microglial changes already at 8 weeks post-surgery, which progressed as a function of time. We found a progressive decrease in microglial surface area (0.9%, n.s., 12.3%, $p=0.0001$ and 17.1%, $p<0.0001$ at 8, 14, and 16 weeks, respectively, one-way ANOVA, $F=15.87$, $p<0.0001$); a progressive decrease in microglial cell volume (7.0%, $p=0.0475$, 27.5%, $p<0.0001$ and 34.0%, $p<0.0001$ at 8, 14, and 16 weeks, respectively, one-way ANOVA, $F=61.99$, $p<0.0001$); a decrease in filament length (10.6%, $p=0.0002$, 12.5%, $p<0.0001$ and 26.1%, $p<0.0001$ at 8, 14, and 16 weeks, respectively, one-way ANOVA, $F=32.42$, $p<0.0001$); a progressive reduction in the number of dendritic branches (17.8%, $p<0.0001$, 21.0%, $p<0.0001$ and 26.6%, $p<0.0001$ at 8, 14, and 16 weeks, respectively, one-way ANOVA, $F=30.06$, $p<0.0001$); a progressive reduction in the number of dendritic segments (24.2%, $p<0.0001$, 26.8%, $p<0.0001$ and 32.2%, $p<0.0001$ at 8, 14, and 16 weeks, respectively, one-way ANOVA, $F=58.72$, $p<0.0001$); a reduction in the number of filament terminals (22.3%, $p<0.0001$, 26.0%, $p<0.0001$ and 28.1%, $p<0.0001$ at 8, 14, and 16 weeks, respectively, one-way ANOVA, $F=49.5$, $p<0.0001$) and a progressive increase in IBA1 intensity (17.4%, $p<0.0001$, 34.4%, $p<0.0001$ and 34.6%, $p<0.0001$ at 8, 14, and 16 weeks, respectively, one-way ANOVA, $F=160.7$, $p<0.0001$). These findings indicate that HF-induced NI in the PVN is evident as early as 8 weeks after the myocardial infarction (MI).

Next, to rule out that HF-induced NI was a rather diffuse inflammatory phenomenon affecting the whole brain, we chose the primary somatosensory cortex (barrel field, S1BF, Fig. 5a, b) as a functionally-unrelated control region and analyzed IBA1-labeled microglia in this structure. We did not observe any significant microglial changes within this region, suggesting that, at least at this stage of HF-induced NI, cortical brain areas might not be affected.

HF-induced delayed NI and morphometric microglial changes in the CeA

Representative confocal images of CeA microglia of sham and HF rats 16-weeks post-surgery are shown in Fig. 6a. In stark contrast to the PVN, except for a slight decrease in filament length, we did not detect any significant changes in microglia morphology 8 weeks after surgery, indicating that HF-induced NI does not affect the CeA at this point in time. However, some changes in microglial morphometric parameters emerged at 14 weeks, which continued to progress at week 16. We found a decrease in

microglial surface area (2.4%, n.s. and 15.6%, $p=0.001$ at 14 and 16 weeks, respectively, one-way ANOVA, $F=5.291$, $p=0.0012$); an initial increase by 21.4%, $p<0.0001$ followed by a later decrease by 12.7%, $p=0.0152$ in microglial cell volume at 14 and 16 weeks, respectively, one-way ANOVA, $F=15.65$, $p<0.0001$; a progressive decrease in filament length (12.0%, $p=0.001$, 10.2%, $p=0.0299$ and 28.3%, $p<0.0001$ at 8, 14 and 16 weeks, respectively, one-way ANOVA, $F=19.87$, $p<0.0001$); a progressive reduction in the number of dendritic branches (10.0%, $p=0.0368$ and 15.1%, $p=0.0033$ at 14 and 16 weeks, respectively, one-way ANOVA, $F=6.8884$, $p=0.0001$); a reduction in the number of dendritic segments (12.1%, $p=0.0057$ and 18.5%, $p=0.0001$ at 14 and 16 weeks, respectively, one-way ANOVA, $F=8.975$, $p<0.0001$); a progressive reduction in the number of filament terminals (15.3%, $p=0.0002$ and 21.0%, $p<0.0001$ at 14 and 16 weeks, respectively, one-way ANOVA, $F=10.78$, $p<0.0001$) and a progressive increase in IBA1 intensity (11.1%, $p<0.0001$ and 25.5%, $p<0.001$ at 14 and 16 weeks, respectively, one-way ANOVA, $F=41.15$, $p<0.0001$, Fig. 6b, c). It is important to note that while we observed an initial increase of microglial cell volume at 14 weeks-post surgery in CeA, at 16 weeks post-surgery the cell volume was drastically decreased compared to the sham group. These findings suggest that during HF, microglia undergo cellular/somatic swelling prior to the retraction of processes and decrease in cellular volume. Taken together, these results indicate that CeA microglia undergo drastic HF-induced morphometric changes, albeit with a delayed time course compared to PVN microglia. The complete overview of all individual values from all groups can be found in Table 1.

HF-induced NI involves microglial deramification and somatic swelling in both PVN and CeA

As stated above, activated microglia have been demonstrated to undergo deramification, a process where microglia retract their processes, lose dendritic complexity and release inflammatory cytokines (42, 52). Thus, to further investigate microglial cell morphometric changes during HF in the PVN and CeA, we performed a Sholl analysis of individually 3D-reconstructed microglial cells in each experimental group. To this end, we superimposed spheres of increasing radius (1 μm increase in radius per step, Fig. 7a) starting at the center of the soma, and measured the number of process intersections that each sphere encountered. We found that in the PVN (Fig. 7b) microglia displayed a significant loss of complexity (indicated by a significantly reduced average number of total Sholl intersections) that occurred in a time-dependent manner (Fig. 7b, 11.1%, $p=0.0142$, 17.1%, $p<0.0001$ and 30.8%, $p<0.0001$ at 8, 14, and 16 weeks, respectively, one-way ANOVA, $F = 32.07$, $p<0.0001$), with changes being already detectable 8 weeks post-surgery, and becoming progressively more deramified at 14- and 16-weeks post-surgery. In the CeA (Fig. 7c), we did not observe such changes at 8- or 14-weeks post-surgery. However, 16-weeks post-surgery, microglia in the CeA displayed significant deramification (sham: 641.3 ± 34 vs. HF 16w: 534.7 ± 25 , $p=0.0002$, one-way ANOVA, $F=8.366$, $p<0.0001$). A recent two-dimensional high throughput study on microglia suggested that detailed morphometric analyses of microglia might be more informative and yielded valuable information leading the authors to coin the terms 'low and high-activity' microglia (53). In accordance with this newly proposed terminology, we classified the different stages of microglia into 'low and high' activity microglia. To quantify the degree of overall microglia activation, we first determined the peak number of Sholl intersections (i.e., the highest numeric value of a sphere intersecting with a microglial process) per individual microglial cell, which in our entire sampled microglia cell population

ranged from 0 to 64 (the higher the number, the more ramified the microglial structure). Using a semi-arbitrary and conservative threshold of <10 to categorize a microglial cell as active, we found 32.5% highly active microglia in the PVN (Fig. 7d) and 30.9% in the CeA (Fig. 7e) of sham rats 14 weeks post-surgery. In the HF rats, we found a significant increase in the number of high activity microglia 8 weeks post-surgery in the PVN (HF 14w: 41.4% vs. sham: 32.5%, $p=0.0125$, one-way ANOVA, $F=25.70$, $p<0.0001$), but not the CeA (31.78%, n.s.). However, 14 weeks post-surgery we found a significant increase in the number of activated microglia in the CeA (38.18%, $p=0.0201$, one-way ANOVA, $F=12.12$, $p<0.0001$), while the number of activated microglia in the PVN had further increased (55.9%, $p=0.001$). In the CeA, the percentage of high activity microglia had further increased 16 weeks post-surgery (HF 16w: 44.0%, $p=0.0163$), which was not the case for the PVN (60.25%, n.s.).

Finally, we analyzed the Sholl distribution curves for sham and HF in the PVN and the CeA at 16-weeks post-surgery and also compared microglia between PVN and CeA in sham animals (Fig. 7f-h). We found significant differences for both the PVN (two-way ANOVA, group: $F(1, 62)=92.09$, $p<0.0001$, Fig. 7f) and the CeA (two-way ANOVA, group: $F(1, 62)=86.93$, $p<0.0001$, Fig. 7g). In the PVN the mean peak number of Sholl intersections was reached at 21 μm distance from the soma for both HF and sham animals, and the mean number of intersections at the peak was significantly different between those groups (sham: 18.5 ± 1.2 intersections vs. HF 16w: 10.2 ± 0.9 intersections, $p<0.0001$). In the CeA, this peak was reached at 22 μm for the sham group and 21 μm for the HF group and was also significantly differed between the two groups (sham: 21.9 ± 1.6 intersections vs. HF 16w: 13.9 ± 1.3 intersections, $p<0.0001$). Interestingly, under control conditions microglial cells in the CeA were significantly more complex than in the PVN (two-way ANOVA, group: $F(1, 62)=77.29$, $p<0.0001$, Fig. 7h), highlighting the morphological heterogeneity among microglia within different brain regions. These findings suggest that microglia in both PVN and CeA undergo drastic morphometric changes and deramification during HF.

A recent study highlighted that in addition to deramification, active microglia display somatic swelling (53), a process thought to coincide with the release of pro-inflammatory cytokines, especially in neurodegeneration (54). Thus, to investigate whether HF-induced NI resulted in somatic microglia swelling, we used our 3D profiler to calculate the somatic volume of individual microglial cells. We found that the average microglial soma volume of sham rats 14 weeks post-surgery was $554.3 \pm 21 \mu\text{m}^3$ for the PVN and $529.0 \pm 41 \mu\text{m}^3$ for the CeA (Fig. 8a-c). We found a time-dependent increase in somatic volume of PVN microglia: 28.2%, $p=0.0008$ and 43.1%, $p<0.0001$ at 14 and 16 weeks, respectively, compared to the respective sham group, one-way ANOVA, $F=14.97$, $p<0.0001$. In the CeA, we found even more drastic time-dependent increases in somatic volume: 41.3%, $p<0.0001$ and 51.2%, $p<0.0001$ at 14 and 16 weeks, respectively, compared to the respective sham group, one-way ANOVA, $F=17.95$, $p<0.0001$. We next sought to investigate whether somatic swelling and microglial deramification were correlated processes or whether they occurred independently in separate microglial subpopulations. Therefore, we correlated soma volume and the total number of Sholl intersections for each microglial cell (Fig. 8d-g). We found that both in sham and HF rats, somatic swelling and deramification were highly correlated processes and this held true for both PVN and CeA ($p<0.0001$ for all cases). Interestingly, we observed apparent

decreases in the slope of the best-fit non-linear regression line (Fig. 8d-g, red lines) between sham and HF rats in both brain regions, which might be indicative of the less polarized (i.e., more homogenous) microglial cell population spectrum in HF rats, resulting from the shift towards a highly active microglial stage. It is important to note that although we found CeA microglia to have a smaller average somata than PVN microglia in sham rats, they surpassed PVN microglia in soma volume at 14 weeks post-surgery. This finding suggests that although somatic swelling and deramification are correlated phenomena, somatic swelling might be initiated earlier and could potentially explain the initial increase in total cell volume in CeA microglia at this time (Fig. 6b, cell volume, HF 14w).

HF induces a morphological A1 astrocyte phenotype in both PVN and CeA

During injury and disease, microglia and astrocytes display intricate interactions that may lead either to neuronal survival or neuronal loss. A recent study showed that activated microglia induce a neurotoxic 'A1' subtype of astrocytes, secreting a currently unknown neurotoxin that results in neuronal cell death (48). A1 astrocytes can be discriminated from the neuroprotective A2 astrocytes not only by the upregulation of genetic markers (47-49, 55), but also by distinct morphological changes, which appear to be similar to those of microglia during NI (56). While retraction of astrocytic processes, hypertrophy and gliosis has been described for astrocytes under various conditions (57), no study – to the best of our knowledge – comprehensively addressed alterations in astrocyte morphology during chronic NI using a three-dimensional reconstruction profiler. Given that NI-induced changes in astrocytes seem to generally follow those observed in microglia (47, 48), we chose to investigate astrocytic changes at 14 weeks post-surgery.

To investigate whether HF-induced NI would result in the induction of the A1 astrocytic phenotype, we first performed conventional 2D z-stack analysis of glial fibrillary acidic protein (GFAP) immunoreactivity in FIJI, but found no differences in either GFAP signal intensity or density (Fig. 9a, b). Next, we performed 3D IMARIS analysis of astrocytes (Fig. 9c) that were immunohistochemically identified by their expression of both GFAP and glutamine synthetase (GluSyn) (Fig. 9d, g). We specifically chose a combination of these two markers because they allowed us to perform a detailed analysis of astrocytic somata and processes, given that GFAP stains mostly processes, but not the soma, while GluSyn predominantly stains the astrocyte soma, but not processes (see Fig. 9i). In HF rats, we found drastic morphological changes in both PVN and CeA astrocytes 14 weeks post-surgery (n=4 rats/group) that included a decrease in surface area (17.2%, $p=0.0009$ and 19.1%, $p=0.0014$, for PVN and CeA, respectively), cell volume (24.4%, $p=0.0003$ and 23.2%, $p=0.0004$, for PVN and CeA, respectively), filament length (19.4%, $p=0.0009$ and 24.6%, $p=0.0001$, for PVN and CeA, respectively) and an increase in soma volume (30.8%, $p<0.0001$ and 18.8%, $p=0.01$, for PVN and CeA, respectively, Fig. 9e, h). In addition, the Sholl distribution analysis revealed significant changes in astrocyte complexity 14-weeks post-surgery for both the PVN (two-way ANOVA, group: $F(1, 81)=76.37$, $p<0.0001$, Fig. 9f) and CeA (two-way ANOVA, group: $F(1, 62)=71.26$, $p<0.0001$, Fig. 9i). Furthermore, we found astrocytes in both the PVN and the CeA of HF rats displayed a significant loss of process complexity, as shown by a significant decrease in the total number of Sholl intersections per astrocyte both in the PVN (18.0%) and the CeA (27.8%, $p<0.0001$ in both cases, Fig. 9j,

k). Fig. 9I shows an isolated PVN astrocyte of a HF rat and subsequent surface reconstruction via IMARIS.

HF induces expression of genes associated with neuroinflammation and A1 astrocyte phenotype in both PVN and CeA

To determine whether the microglial/astrocyte morphometric changes observed in HF rats also corresponded with a genetic profile associated to NI and/or a shift to an A1 astrocyte phenotype, we performed qPCR of mRNA transcripts of various genes classically associated to NI, as well as several A2 and A1 astrocyte-related genes. We analyzed mRNA levels of IBA1 and GFAP, cytokines (TNF- α , IL-1 β and IL-6), A1 astrocyte markers (Serping1 and C3) and A2 astrocyte markers (Tm4sf1 and Sphk1) in micropunches obtained from the PVN and CeA of sham and HF rats at the same time points (8w and 14w) at which the morphometric studies were performed.

In the PVN, we found significant changes in tested genes already at 8 weeks post-surgery (n=5 per group, pooled): an increase in IBA1 (1.344-fold, p=0.0006), cytokines (IL-1 β : 3.51-fold, p=0.0163; IL-6: 1.522-fold, p=0.0067 and TNF- α : 3.117-fold, p=0.0016) and A1 astrocyte markers (Serping1: 2.767-fold, p=0.017 and C3: 1.127-fold, p=0.0323) as well as a significant decrease in GFAP (-1.583-fold, p=0.0006) and A2 astrocyte markers (Tm4sf1: -1.373-fold, p=0.0005 and Sphk1: -1.17-fold, p=0.0005, Fig. 10a). When we analyzed the genes again 14 weeks post-surgery (Fig. 10b) (n=4/group, pooled), the qPCR of PVN tissue yielded comparable results: IBA1: 1.683-fold, p=0.0089; GFAP: -1.563, p=0.0006; IL-1 β : 3.533-fold, p=0.0134; IL-6: 1.62-fold, p=0.0045; TNF- α : 2.433-fold, p=0.0344; Serping1: 4.2-fold, p=0.0042; C3: 1.387-fold, p=0.0237; Tm4sf1: -1.897, p<0.0001, Sphk1: -1.333, p=0.0012).

In the CeA we found only GFAP (-1.249-fold, p=0.0004), IL-1 β (2.383-fold, p=0.0291) and TNF- α (2.367-fold, p=0.004) to be significantly altered 8 weeks post-surgery (Fig. 10c). However, 14 weeks post-surgery (Fig. 10d) we found significant differences in all tested genes, which were comparable to those observed in the PVN: IBA1 (1.433-fold, p=0.0039), GFAP (-1.323-fold, p=0.0002), IL-1 β (2.893-fold, p=0.0066), IL-6 (1.757-fold, p=0.0035), TNF- α (2.72-fold, p<0.0001), Serping1 (5.033-fold, p=0.0009), C3 (1.243-fold, p=0.0404), Tm4sf1 (-1.738-fold, p=0.0004) and Sphk1 (-1.57-fold, p=0.0009). We did not observe significant changes either at 8 weeks or 14 weeks post-surgery in the prelimbic cortex (PLC, Fig. 10e, f), suggesting that cortical areas might not be affected by HF-induced NI at this point in time.

Discussion

Heart failure-induced NI and its physiological and behavioral correlates

CVDs including stroke and HF are the leading cause of deaths worldwide, and affected individuals suffer from severe physiological and psychological impairments (1). While compounds like angiotensin converting enzyme inhibitors, angiotensin receptor blockers, mineralocorticoid receptor antagonists or β -blockers have been successfully used to treat the physiological symptoms of HF patients with reduced EF (58), little to no treatment is available for HF-induced mood and anxiety disorders. In fact, recent studies

suggest that the classical use of selective serotonin reuptake inhibitors (SSRIs) may not be an efficient way to relieve depression symptoms in HF patients (59, 60). Importantly, NI and oxidative stress in the PVN and the rostral-lateral medulla have been reported in rats with HF and neurogenic hypertension (25, 61, 62). It is well-established that inflammation and activation of the renin-angiotensin system (RAS) drastically increases sympathetic drive, thereby creating a vicious circle with debilitating effects on affected individuals (63). Moreover, intracerebroventricular infusions of minocycline, an anti-inflammatory antibiotic that inhibits microglia cell activation, resulted in significant attenuation of mean arterial pressure and cardiac hypertrophy (61). These changes were accompanied by a reduction in the total number of activated microglia as well as reduced mRNA levels for IL-1 β , IL-6 and TNF- α (61). Taken together, these previous studies pinpoint NI, particularly microglial cell activation within the PVN, as a key underlying pathophysiological mechanism contributing to the sympathohumoral and cardiovascular complications associated with HF (23-26). Given that the PVN is a key regulatory structure involved in the integration of behavioral, cardiovascular and neuroendocrine homeostatic responses (64-66), and is richly interconnected with a plethora of brain regions (32, 67-69), including the amygdala, it is reasonable to speculate that NI could also contribute to mood and anxiety disorders associated to HF. In fact, PVN-amygdala connectivity is well-established (32, 67-69) and the release of various PVN-synthesized neuropeptides within the amygdala has been shown to directly modulate aggression, fear and depression (37, 38, 70). However, to the best of our knowledge, no previous study demonstrated that HF-induced NI within the CeA results in a drastic shift from a low to a high activity state of the microglial cell population.

Microglia cell activation in the paraventricular nucleus and central amygdala in heart failure rats

Microglia, the resident immune cells of the brain parenchyma are among the first responding cells during injury, cell death or unwanted intruders that might access the brain due to a compromised blood-brain-barrier (40, 42, 43, 52, 71). Microglia represent a major component in the immune response and participate in the neuroinflammatory response largely via the release pro-inflammatory cytokines (42, 52). During NI, microglia undergo an astonishing morphological transition from a highly ramified to a deramified state, retracting their fine processes and experiencing an overall reduction in cell volume (42, 43, 72). Although it seems evident that a comprehensive knowledge of microglial deramification is of paramount importance, very little is known about the precise series of events that ultimately lead to deramification, highlighting the need for tools that allow a detailed morphometric analysis of microglial remodeling. While other laboratories employed comparable approaches for the reconstruction of microglia under various conditions using different software (73-75), these approaches are very time-consuming (80 minutes or more per z-stack), and could result in over- and/or undersampling given that fused (microglia recognized as one entity by the software) or cut microglia (somata or processes cut by either the x,y or z axis) are included in the analysis. These limitations are largely overcome by our glial profiler based on the IMARIS software which allows for an unbiased, rapid, and fully automated reconstruction and morphometric analysis of individually identified microglial cell. Moreover, our profiler identifies and either separates or eliminates incomplete or fused microglial profiles. While this is not the first study to implement IMARIS analysis for three-dimensional reconstruction of microglia (76, 77), our in-depth analysis of activated microglia and their morphometric transition from low an activity to a high

activity state in the context of the progression of a disease model represents, to the best of our knowledge, an unprecedented approach. To specifically probe for HF-induced NI, we stained brain slices with IBA1 and used our newly developed 3D profiler as a comprehensive tool for the assessment of microglial structural remodeling in a well-established experimental model of HF. Morphometric analysis of microglia is superior to classical IHC-based quantification, as it not only provides information about overall microglia-related immunoreactivity density and intensity, but also provides insights into a variety of specific morphological changes within individually identified microglial cell, such as somatic swelling and process remodeling (53). With our 3D profiler, we were able to detect drastic time-dependent microglia morphological changes in HF rats including filament shortening, deramification and somatic swelling in both PVN and CeA. These changes are widely accepted as indicators of microglial cell activation (42, 43, 52, 53, 73). Importantly, a conventional 2D analysis of IBA1-stained microglia failed to find significant differences in microglia morphology further supporting the higher sensitivity and precision of this novel approach. We found that both in PVN and CeA, microglial cell remodeling worsened over time (Figs. 4, 6), which is highlighted in part by a progressive increase in the number of activated microglia (Fig. 7) and a shift of the microglial population towards a highly deramified microglial phenotype. Although the retraction of microglial processes and somatic swelling were highly correlated (Fig. 8), we found an initial increase in total cell volume in the CeA (14w, Fig. 6) suggesting that somatic swelling might precede the deramification. Our data also suggest that HF-induced microglial cell changes were not representative of a diffused NI phenomenon globally affecting the brain, given that non-related regions, such as S1BF and the PLC (Fig. 5, 10) were not affected, at least at this time point of the disease. Finally, it is important to note that we found significant differences in cell volume, surface area and IBA1 intensity when we compared microglial cells between the PVN and the CeA in sham rats (Fig. 7). These results are in line with previous studies performed both in rodents and humans supporting a high degree of variability of microglial phenotypes that might depend on age, brain region and pathophysiological condition (43, 78, 79).

Region-specific differences and time-dependency of heart failure-induced neuroinflammation

We found that microglial cell remodeling in the PVN is present already at 8w post-surgery, while microglial changes in the CeA started to unfold around the 14-week mark. While our study demonstrated for the first HF-induced microglial cell remodeling in the CeA, a major finding was that these changes occurred in a delayed manner compared to the PVN. These time-dependent microglial structural changes were consistent, and correlated as well with qPCR analysis of pro-inflammatory markers, such as TNF- α , IL-1 β and IL-6, which in the PVN were already drastically elevated at 8w, while in the CeA most markers became significantly elevated at 14w post-surgery. These results further support the previously established relationship between microglial cell morphological changes with the release of proinflammatory cytokines (42, 43).

As stated above, a large body of evidence supports a key role for the PVN in the onset and maintenance of cardiovascular dysregulation in HF (11, 18-22). Thus, the time-dependent differences in microglial cell activation and pro-inflammatory markers between the PVN and the amygdala are in line with the fact

sympathohumoral and cardiovascular manifestations in HF precede the mood and cognitive deficits associated with this disease (58, 80, 81). HF-induced cognitive impairments in both rats and mice have been extensively studied (82, 83) and while it is well established that the PVN is a main neuronal substrate contributing to mood regulation, our studies provide an indirect evidence that NI within the amygdala may constitute a neuronal substrate contributing to HF-induced mood deficits. A recent study showed that the microglia inhibitor minocycline improved depression-like behavior in HF rats (84). However, the authors performed oral delivery of minocycline so that the precise site of action within the brain underlying the improvement of the depression-like behavior could not to be determined. Moreover, anti-inflammatory compounds showed good clinical efficacies in attenuating levels of TNF- α and IL-1 β and improving disease outcome of various neuropathologies, psychiatric disorders, including Alzheimer's disease (85-87). Still, further studies are clearly necessary to demonstrate that NI within the CeA contributes to HF-induced depression-like behavioral changes. The mechanisms underlying the time course differences between the HF-induced NI in PVN and CeA could be manifold and not mutually exclusive. Based on the tightly coupled interaction between the PVN and the amygdala (32, 67-69), NI in the amygdala could be triggered by the exaggerated neuronal activity in the PVN reported in HF (21, 22, 88, 89). This is in line with previous studies showing that aberrant neuronal activity could result in the release of damage-associated molecules, leading to microglia activation (90, 91). Recent studies also support the ability of inflammatory cytokines to diffuse in the extracellular space (92-94). Thus, the delay for NI onset in the amygdala could be due to the slow lateral diffusion of cytokines initially originating in the PVN. Finally, the delay may also be due to differential responsiveness of PVN and amygdala microglial cell populations to the same noxious stimulus (i.e. HF-associated hypoxia) and/or differences in blood-brain-barrier integrity, between the PVN and CeA during disease states, which could result in region-specific permeability differences, as we recently showed to be the case during hypertension (95). Clearly, future studies are warranted to address the precise mechanisms underlying the differential and region-specific time course of microglia cell activation during HF.

Morphological changes in PVN and CeA astrocytes and shift towards A1 phenotype

The intricate interaction between microglia and astrocytes during NI is well-established (56, 96, 97). Microglial cells release various pro-inflammatory molecules upon injury (98) or as a result of the general immune response (99), which in turn triggers specific astrocytic responses. Astrocytes can release osomucoid-2 to inhibit microglial activation, block the chemokine receptor type 5 of the microglial membrane, downregulate the inflammatory response or further promote neuroinflammation and neurodegeneration (97). This bidirectional interaction allows an efficient and tailored response to various potentially harmful threats that the brain might be exposed to. Recent studies suggested the classification of astrocytes into two categories: A1 (pro-inflammatory, neurotoxic) and A2 (anti-inflammatory, neuroprotective) astrocytes (47-49). During the transition from the A2 to A1 phenotype, astrocytes are thought to undergo morphometric changes comparable to those observed in microglia. Based on this, we applied a 3D morphometric analysis in analogy to our microglial analysis to the study of astrocytes in the PVN and CeA of HF rats. Similar to what we found with microglial cells, while a conventional 2D analysis of GFAP immunoreactivity failed to demonstrate any changes in PVN

astrocytes of HF rats, our results with the 3D profiler demonstrated significant morphological changes in both PVN and CeA astrocytes during HF. Importantly, these morphometric changes were accompanied by the upregulation of A1-specific (Serping1, C3) and downregulation of A2-specific (Tm4sf1 and Sphk1) astrocyte markers. Taken together, these results indicate that HF promotes a shift in astrocyte phenotype from A2 to A1 both in the PVN and CeA, contributing thus along microglial cells to the overall NI state in this disease. It is important to note that while we analyzed changes in astrocyte morphology only at 14 weeks post-surgery, the time differences in the A1/A2 mRNA markers also support a time-dependent difference between PVN and CeA in astrocyte changes that coincides with the time course of microglia changes. Interestingly, we found a significantly decreased GFAP mRNA levels in HF rats of both PVN and CeA. While these findings might seem contrary to the general notion that GFAP protein levels are increased in A1 astrocytes, recent studies suggest that GFAP might not be the best marker for astrocyte reactivity (47) and highlight that the relationship between reactive astrocytes and GFAP levels might have been oversimplified (100). Taken together, our findings suggest that HF-induced NI not only alters the microglial environment in affected brain regions, but rather has far-reaching consequences affecting astrocytes and potentially even neurons due to astrocyte-induced neurotoxicity (47, 48). Additional studies are needed to determine whether the HF-induced A1 astrocyte phenotype in the CeA becomes neurotoxic and if so, what subpopulation of CeA neurons might be affected

Conclusion

In summary, in the present study we implemented a novel and improved morphometric imaging approach to assess precise microglial and astrocyte structural remodeling in different brain regions during the progression of heart failure. We provide evidence that in addition to the previously described NI observed in the hypothalamic PVN, known to be implicated in sympathohumoral activation during this disease, microglia and astrocytes within the central amygdala (CeA) also undergo drastic structural remodeling. These structural changes are indicative of glial shift towards an activated and neurotoxic phenotype respectively, a finding supported also by an increased expression of pro-inflammatory cytokines. Importantly, our results show that NI in the CeA manifested with a delayed time course with respect to the PVN. Taken together, our studies support the idea that NI in the amygdala may contribute to emotional and cognitive deficits commonly observed at later stages during the course of HF, standing thus as a potential novel target for alleviating comorbid mood disorders in this prevalent disease (2, 4, 101).

Abbreviations

C3 – Complement component 3, CeA – Central amygdala, CeL – Lateral subdivision of the central amygdala, CVDs – Cardiovascular diseases, GFAP – Glial fibrillary acidic protein, GluSyn – Glutamine Synthetase, HF – heart failure, IL – Interleukin, MI – Myocardial infarction, NI – Neuroinflammation, OT – Oxytocin, PLC – Prelimbic cortex, Serping1 – C1-inhibitor gene, Sphk1 – Sphingosine kinase 1, SSRIs – Selective serotonin reuptake inhibitors, Tm4sf1 – Transmembrane 4 L6 family member 1, TNF-a - Tumor necrosis factor a.

Declarations

Acknowledgements

We thank Atit Patel and Dr. Daniel Cox for their assistance with the qPCR. We also thank Dr. Anne Murphy for kindly providing the GFAP antibody.

Authors' contributions

FA performed immunohistochemistry, IMARIS reconstruction, analyzed the data and wrote the manuscript; FA and HCFN performed qPCR; HCFN and RKR performed the coronary artery ligation surgery and echocardiographic assessment of EF; MR developed the IMARIS microglial profiler; JES supervised the experiments, designed the study and edited the manuscript. All authors critically reviewed the manuscript and approved the final version for publication.

Funding

This work was supported by DFG Postdoc Fellowship AL 2466/1-1 to FA; National Heart, Lung, and Blood Institute Grant NIH HL090948, and funding provided by the Center for Neuroinflammation and Cardiometabolic Diseases (CNCD).

Availability of data and materials

The datasets used and/or analyzed in the current study are available from the corresponding author upon reasonable request.

Ethics approval and consent to participate

All experiments were performed following the approval of the Ethics Committee for Animal Experiments at Georgia State University (IACUC protocol # A18003). All efforts were made to minimize the suffering of the animals and reduce their total number.

Consent for publication

Not applicable.

Competing interests

The author declare that they have no competing interests.

References

1. Group WCRCW. World Health Organization cardiovascular disease risk charts: revised models to estimate risk in 21 global regions. *Lancet Glob Health*. 2019;7(10):e1332-e45.

2. Mbakwem A, Aina F, Amadi C. Expert Opinion-Depression in Patients with Heart Failure: Is Enough Being Done? *Card Fail Rev.* 2016;2(2):110-2.
3. Parissis JT, Fountoulaki K, Paraskevaïdis I, Kremastinos D. Depression in chronic heart failure: novel pathophysiological mechanisms and therapeutic approaches. *Expert Opin Investig Drugs.* 2005;14(5):567-77.
4. Rustad JK, Stern TA, Hebert KA, Musselman DL. Diagnosis and treatment of depression in patients with congestive heart failure: a review of the literature. *Prim Care Companion CNS Disord.* 2013;15(4).
5. Konstam V, Moser DK, De Jong MJ. Depression and anxiety in heart failure. *J Card Fail.* 2005;11(6):455-63.
6. Rutledge T, Reis VA, Linke SE, Greenberg BH, Mills PJ. Depression in heart failure a meta-analytic review of prevalence, intervention effects, and associations with clinical outcomes. *J Am Coll Cardiol.* 2006;48(8):1527-37.
7. Hammond CA, Blades NJ, Chaudhry SI, Dodson JA, Longstreth WT, Jr., Heckbert SR, et al. Long-Term Cognitive Decline After Newly Diagnosed Heart Failure: Longitudinal Analysis in the CHS (Cardiovascular Health Study). *Circ Heart Fail.* 2018;11(3):e004476.
8. Frey A, Popp S, Post A, Langer S, Lehmann M, Hofmann U, et al. Experimental heart failure causes depression-like behavior together with differential regulation of inflammatory and structural genes in the brain. *Front Behav Neurosci.* 2014;8:376.
9. Prickaerts J, Raaijmakers W, Blokland A. Effects of myocardial infarction and captopril therapy on anxiety-related behaviors in the rat. *Physiol Behav.* 1996;60(1):43-50.
10. Schoemaker RG, Smits JF. Behavioral changes following chronic myocardial infarction in rats. *Physiol Behav.* 1994;56(3):585-9.
11. Benarroch EE. Paraventricular nucleus, stress response, and cardiovascular disease. *Clin Auton Res.* 2005;15(4):254-63.
12. Coote JH, Yang Z, Pyner S, Deering J. Control of sympathetic outflows by the hypothalamic paraventricular nucleus. *Clin Exp Pharmacol Physiol.* 1998;25(6):461-3.
13. Kannan H, Yamashita H. Electrophysiological study of paraventricular nucleus neurons projecting to the dorsomedial medulla and their response to baroreceptor stimulation in rats. *Brain Res.* 1983;279(1-2):31-40.
14. Ranson RN, Motawei K, Pyner S, Coote JH. The paraventricular nucleus of the hypothalamus sends efferents to the spinal cord of the rat that closely appose sympathetic preganglionic neurones projecting to the stellate ganglion. *Exp Brain Res.* 1998;120(2):164-72.
15. Althammer F, Grinevich V. Diversity of oxytocin neurons: beyond magno- and parvocellular cell types? *J Neuroendocrinol.* 2017.
16. Stern JE. Neuroendocrine-autonomic integration in the paraventricular nucleus: novel roles for dendritically released neuropeptides. *J Neuroendocrinol.* 2015;27(6):487-97.

17. Atasoy D, Betley JN, Su HH, Sternson SM. Deconstruction of a neural circuit for hunger. *Nature*. 2012;488(7410):172-7.
18. Patel KP. Role of paraventricular nucleus in mediating sympathetic outflow in heart failure. *Heart Fail Rev*. 2000;5(1):73-86.
19. Pyner S. The paraventricular nucleus and heart failure. *Exp Physiol*. 2014;99(2):332-9.
20. Ramchandra R, Hood SG, Frithiof R, McKinley MJ, May CN. The role of the paraventricular nucleus of the hypothalamus in the regulation of cardiac and renal sympathetic nerve activity in conscious normal and heart failure sheep. *J Physiol*. 2013;591(1):93-107.
21. Biancardi VC, Son SJ, Sonner PM, Zheng H, Patel KP, Stern JE. Contribution of central nervous system endothelial nitric oxide synthase to neurohumoral activation in heart failure rats. *Hypertension*. 2011;58(3):454-63.
22. Potapenko ES, Biancardi VC, Florschütz RM, Ryu PD, Stern JE. Inhibitory-excitatory synaptic balance is shifted toward increased excitation in magnocellular neurosecretory cells of heart failure rats. *J Neurophysiol*. 2011;106(3):1545-57.
23. Najjar F, Ahmad M, Lagace D, Leenen FHH. Sex differences in depression-like behavior and neuroinflammation in rats post-MI: role of estrogens. *Am J Physiol Heart Circ Physiol*. 2018;315(5):H1159-H73.
24. Najjar F, Ahmad M, Lagace D, Leenen FHH. Role of Myocardial Infarction-Induced Neuroinflammation for Depression-Like Behavior and Heart Failure in Ovariectomized Female Rats. *Neuroscience*. 2019;415:201-14.
25. Kang YM, Ma Y, Elks C, Zheng JP, Yang ZM, Francis J. Cross-talk between cytokines and renin-angiotensin in hypothalamic paraventricular nucleus in heart failure: role of nuclear factor-kappaB. *Cardiovasc Res*. 2008;79(4):671-8.
26. Yu Y, Wei SG, Weiss RM, Felder RB. Angiotensin II Type 1a Receptors in the Subfornical Organ Modulate Neuroinflammation in the Hypothalamic Paraventricular Nucleus in Heart Failure Rats. *Neuroscience*. 2018;381:46-58.
27. Wotjak CT, Kubota M, Liebsch G, Montkowski A, Holsboer F, Neumann I, et al. Release of vasopressin within the rat paraventricular nucleus in response to emotional stress: a novel mechanism of regulating adrenocorticotrophic hormone secretion? *J Neurosci*. 1996;16(23):7725-32.
28. Herman JP, Tasker JG. Paraventricular Hypothalamic Mechanisms of Chronic Stress Adaptation. *Front Endocrinol (Lausanne)*. 2016;7:137.
29. Myers B, McKlveen JM, Herman JP. Glucocorticoid actions on synapses, circuits, and behavior: implications for the energetics of stress. *Front Neuroendocrinol*. 2014;35(2):180-96.
30. Townsend JD, Eberhart NK, Bookheimer SY, Eisenberger NI, Foland-Ross LC, Cook IA, et al. fMRI activation in the amygdala and the orbitofrontal cortex in unmedicated subjects with major depressive disorder. *Psychiatry Res*. 2010;183(3):209-17.
31. Young KD, Siegle GJ, Zotev V, Phillips R, Misaki M, Yuan H, et al. Randomized Clinical Trial of Real-Time fMRI Amygdala Neurofeedback for Major Depressive Disorder: Effects on Symptoms and

- Autobiographical Memory Recall. *Am J Psychiatry*. 2017;174(8):748-55.
32. LeDoux J. The amygdala. *Curr Biol*. 2007;17(20):R868-74.
 33. LeDoux J. The emotional brain, fear, and the amygdala. *Cell Mol Neurobiol*. 2003;23(4-5):727-38.
 34. LeDoux JE. Emotion circuits in the brain. *Annu Rev Neurosci*. 2000;23:155-84.
 35. Sobota R, Mihara T, Forrest A, Featherstone RE, Siegel SJ. Oxytocin reduces amygdala activity, increases social interactions, and reduces anxiety-like behavior irrespective of NMDAR antagonism. *Behav Neurosci*. 2015;129(4):389-98.
 36. Labuschagne I, Phan KL, Wood A, Angstadt M, Chua P, Heinrichs M, et al. Oxytocin attenuates amygdala reactivity to fear in generalized social anxiety disorder. *Neuropsychopharmacology*. 2010;35(12):2403-13.
 37. Hasan MT, Althammer F, Silva da Gouveia M, Goyon S, Eliava M, Lefevre A, et al. A Fear Memory Engram and Its Plasticity in the Hypothalamic Oxytocin System. *Neuron*. 2019;103(1):133-46 e8.
 38. Knobloch HS, Charlet A, Hoffmann LC, Eliava M, Khrulev S, Cetin AH, et al. Evoked axonal oxytocin release in the central amygdala attenuates fear response. *Neuron*. 2012;73(3):553-66.
 39. Han RT, Kim YB, Park EH, Kim JY, Ryu C, Kim HY, et al. Long-Term Isolation Elicits Depression and Anxiety-Related Behaviors by Reducing Oxytocin-Induced GABAergic Transmission in Central Amygdala. *Front Mol Neurosci*. 2018;11:246.
 40. Nimmerjahn A, Kirchhoff F, Helmchen F. Resting microglial cells are highly dynamic surveillants of brain parenchyma in vivo. *Science*. 2005;308(5726):1314-8.
 41. Raivich G. Like cops on the beat: the active role of resting microglia. *Trends Neurosci*. 2005;28(11):571-3.
 42. Prinz M, Jung S, Priller J. Microglia Biology: One Century of Evolving Concepts. *Cell*. 2019;179(2):292-311.
 43. Prinz M, Priller J. Microglia and brain macrophages in the molecular age: from origin to neuropsychiatric disease. *Nat Rev Neurosci*. 2014;15(5):300-12.
 44. Morrison HW, Filosa JA. A quantitative spatiotemporal analysis of microglia morphology during ischemic stroke and reperfusion. *J Neuroinflammation*. 2013;10:4.
 45. Stratoulis V, Venero JL, Tremblay ME, Joseph B. Microglial subtypes: diversity within the microglial community. *EMBO J*. 2019;38(17):e101997.
 46. Colombo E, Farina C. Astrocytes: Key Regulators of Neuroinflammation. *Trends Immunol*. 2016;37(9):608-20.
 47. Liddelow SA, Barres BA. Reactive Astrocytes: Production, Function, and Therapeutic Potential. *Immunity*. 2017;46(6):957-67.
 48. Liddelow SA, Guttenplan KA, Clarke LE, Bennett FC, Bohlen CJ, Schirmer L, et al. Neurotoxic reactive astrocytes are induced by activated microglia. *Nature*. 2017;541(7638):481-7.
 49. Clarke LE, Liddelow SA, Chakraborty C, Munch AE, Heiman M, Barres BA. Normal aging induces A1-like astrocyte reactivity. *Proc Natl Acad Sci U S A*. 2018;115(8):E1896-E905.

50. Tassoni A, Farkhondeh V, Itoh Y, Itoh N, Sofroniew MV, Voskuhl RR. The astrocyte transcriptome in EAE optic neuritis shows complement activation and reveals a sex difference in astrocytic C3 expression. *Sci Rep.* 2019;9(1):10010.
51. Zamanian JL, Xu L, Foo LC, Nouri N, Zhou L, Giffard RG, et al. Genomic analysis of reactive astrogliosis. *J Neurosci.* 2012;32(18):6391-410.
52. Butovsky O, Weiner HL. Microglial signatures and their role in health and disease. *Nat Rev Neurosci.* 2018;19(10):622-35.
53. Davis BM, Salinas-Navarro M, Cordeiro MF, Moons L, De Groef L. Characterizing microglia activation: a spatial statistics approach to maximize information extraction. *Sci Rep.* 2017;7(1):1576.
54. Hickman S, Izzy S, Sen P, Morsett L, El Khoury J. Microglia in neurodegeneration. *Nat Neurosci.* 2018;21(10):1359-69.
55. Neal M, Luo J, Harischandra DS, Gordon R, Sarkar S, Jin H, et al. Prokineticin-2 promotes chemotaxis and alternative A2 reactivity of astrocytes. *Glia.* 2018;66(10):2137-57.
56. Burda JE, Sofroniew MV. Seducing astrocytes to the dark side. *Cell Res.* 2017;27(6):726-7.
57. Li T, Chen X, Zhang C, Zhang Y, Yao W. An update on reactive astrocytes in chronic pain. *J Neuroinflammation.* 2019;16(1):140.
58. Metra M, Teerlink JR. Heart failure. *Lancet.* 2017;390(10106):1981-95.
59. Rajeswaran T, Plymen CM, Doherty AM. The effect of antidepressant medications in the management of heart failure on outcomes: mortality, cardiovascular function and depression - a systematic review. *Int J Psychiatry Clin Pract.* 2018;22(3):164-9.
60. Ricco J, Benson J, Prasad S. PURLs: SSRIs for depression/heart failure patients? Not so fast. *J Fam Pract.* 2017;66(9):564-7.
61. Shi P, Diez-Freire C, Jun JY, Qi Y, Katovich MJ, Li Q, et al. Brain microglial cytokines in neurogenic hypertension. *Hypertension.* 2010;56(2):297-303.
62. Wu KL, Chan SH, Chan JY. Neuroinflammation and oxidative stress in rostral ventrolateral medulla contribute to neurogenic hypertension induced by systemic inflammation. *J Neuroinflammation.* 2012;9:212.
63. Diaz HS, Toledo C, Andrade DC, Marcus NJ, Rio RD. Neuroinflammation in heart failure: NEW insights for an old disease. *J Physiol.* 2019.
64. Swanson LW, Kuypers HG. The paraventricular nucleus of the hypothalamus: cytoarchitectonic subdivisions and organization of projections to the pituitary, dorsal vagal complex, and spinal cord as demonstrated by retrograde fluorescence double-labeling methods. *J Comp Neurol.* 1980;194(3):555-70.
65. Swanson LW, Sawchenko PE. Paraventricular nucleus: a site for the integration of neuroendocrine and autonomic mechanisms. *Neuroendocrinology.* 1980;31(6):410-7.
66. Guyenet PG. The sympathetic control of blood pressure. *Nat Rev Neurosci.* 2006;7(5):335-46.

67. Kim TK, Han PL. Functional Connectivity of Basolateral Amygdala Neurons Carrying Orexin Receptors and Melanin-concentrating Hormone Receptors in Regulating Sociability and Mood-related Behaviors. *Exp Neurobiol.* 2016;25(6):307-17.
68. Pittman QJ, Blume HW, Renaud LP. Connections of the hypothalamic paraventricular nucleus with the neurohypophysis, median eminence, amygdala, lateral septum and midbrain periaqueductal gray: an electrophysiological study in the rat. *Brain Res.* 1981;215(1-2):15-28.
69. Huber D, Veinante P, Stoop R. Vasopressin and oxytocin excite distinct neuronal populations in the central amygdala. *Science.* 2005;308(5719):245-8.
70. Bosch OJ, Neumann ID. Both oxytocin and vasopressin are mediators of maternal care and aggression in rodents: from central release to sites of action. *Horm Behav.* 2012;61(3):293-303.
71. Thurgur H, Pinteaux E. Microglia in the Neurovascular Unit: Blood-Brain Barrier-microglia Interactions After Central Nervous System Disorders. *Neuroscience.* 2019;405:55-67.
72. Lannes N, Eppler E, Etemad S, Yotovskii P, Filgueira L. Microglia at center stage: a comprehensive review about the versatile and unique residential macrophages of the central nervous system. *Oncotarget.* 2017;8(69):114393-413.
73. Heindl S, Gesierich B, Benakis C, Llovera G, Duering M, Liesz A. Automated Morphological Analysis of Microglia After Stroke. *Front Cell Neurosci.* 2018;12:106.
74. Xu H, Gelyana E, Rajsombath M, Yang T, Li S, Selkoe D. Environmental Enrichment Potently Prevents Microglia-Mediated Neuroinflammation by Human Amyloid beta-Protein Oligomers. *J Neurosci.* 2016;36(35):9041-56.
75. Karperien A, Ahammer H, Jelinek HF. Quantitating the subtleties of microglial morphology with fractal analysis. *Front Cell Neurosci.* 2013;7:3.
76. Erny D, Hrabé de Angelis AL, Jaitin D, Wieghofer P, Staszewski O, David E, et al. Host microbiota constantly control maturation and function of microglia in the CNS. *Nat Neurosci.* 2015;18(7):965-77.
77. VanRyzin JW, Marquardt AE, Argue KJ, Vecchiarelli HA, Ashton SE, Arambula SE, et al. Microglial Phagocytosis of Newborn Cells Is Induced by Endocannabinoids and Sculptures Sex Differences in Juvenile Rat Social Play. *Neuron.* 2019;102(2):435-49 e6.
78. Dubbelaar ML, Kracht L, Eggen BJL, Boddeke E. The Kaleidoscope of Microglial Phenotypes. *Front Immunol.* 2018;9:1753.
79. Bottcher C, Schlickeiser S, Sneeboer MAM, Kunkel D, Knop A, Paza E, et al. Human microglia regional heterogeneity and phenotypes determined by multiplexed single-cell mass cytometry. *Nat Neurosci.* 2019;22(1):78-90.
80. Leto L, Feola M. Cognitive impairment in heart failure patients. *J Geriatr Cardiol.* 2014;11(4):316-28.
81. Celutkiene J, Vaitkevicius A, Jakstiene S, Jatuzis D. Expert Opinion-Cognitive Decline in Heart Failure: More Attention is Needed. *Card Fail Rev.* 2016;2(2):106-9.

82. Toledo C, Lucero C, Andrade DC, Diaz HS, Schwarz KG, Pereyra KV, et al. Cognitive impairment in heart failure is associated with altered Wnt signaling in the hippocampus. *Aging (Albany NY)*. 2019;11(16):5924-42.
83. Hay M, Vanderah TW, Samareh-Jahani F, Constantopoulos E, Uprety AR, Barnes CA, et al. Cognitive impairment in heart failure: A protective role for angiotensin-(1-7). *Behav Neurosci*. 2017;131(1):99-114.
84. Wang HW, Ahmad M, Jadayel R, Najjar F, Lagace D, Leenen FHH. Inhibition of inflammation by minocycline improves heart failure and depression-like behaviour in rats after myocardial infarction. *PLoS One*. 2019;14(6):e0217437.
85. Lurie DI. An Integrative Approach to Neuroinflammation in Psychiatric disorders and Neuropathic Pain. *J Exp Neurosci*. 2018;12:1179069518793639.
86. Shal B, Ding W, Ali H, Kim YS, Khan S. Anti-neuroinflammatory Potential of Natural Products in Attenuation of Alzheimer's Disease. *Front Pharmacol*. 2018;9:548.
87. Gupta N, Shyamasundar S, Patnala R, Karthikeyan A, Arumugam TV, Ling EA, et al. Recent progress in therapeutic strategies for microglia-mediated neuroinflammation in neuropathologies. *Expert Opin Ther Targets*. 2018;22(9):765-81.
88. Roy RK, Augustine RA, Brown CH, Schwenke DO. Activation of oxytocin neurons in the paraventricular nucleus drives cardiac sympathetic nerve activation following myocardial infarction in rats. *Commun Biol*. 2018;1:160.
89. Zheng H, Li YF, Wang W, Patel KP. Enhanced angiotensin-mediated excitation of renal sympathetic nerve activity within the paraventricular nucleus of anesthetized rats with heart failure. *Am J Physiol Regul Integr Comp Physiol*. 2009;297(5):R1364-74.
90. Wohleb ES. Neuron-Microglia Interactions in Mental Health Disorders: "For Better, and For Worse". *Front Immunol*. 2016;7:544.
91. Nair A, Bonneau RH. Stress-induced elevation of glucocorticoids increases microglia proliferation through NMDA receptor activation. *J Neuroimmunol*. 2006;171(1-2):72-85.
92. Tchelingirian JL, Quinonero J, Booss J, Jacque C. Localization of TNF alpha and IL-1 alpha immunoreactivities in striatal neurons after surgical injury to the hippocampus. *Neuron*. 1993;10(2):213-24.
93. Vitkovic L, Konsman JP, Bockaert J, Dantzer R, Homburger V, Jacque C. Cytokine signals propagate through the brain. *Mol Psychiatry*. 2000;5(6):604-15.
94. Stojkovic T, Colin C, Le Saux F, Jacque C. Specific pattern of nitric oxide synthase expression in glial cells after hippocampal injury. *Glia*. 1998;22(4):329-37.
95. Biancardi VC, Stern JE. Compromised blood-brain barrier permeability: novel mechanism by which circulating angiotensin II signals to sympathoexcitatory centres during hypertension. *J Physiol*. 2016;594(6):1591-600.
96. Sofroniew MV. Astrocyte barriers to neurotoxic inflammation. *Nat Rev Neurosci*. 2015;16(5):249-63.

97. Jha MK, Jo M, Kim JH, Suk K. Microglia-Astrocyte Crosstalk: An Intimate Molecular Conversation. *Neuroscientist*. 2019;25(3):227-40.
98. Bellver-Landete V, Bretheau F, Mailhot B, Vallieres N, Lessard M, Janelle ME, et al. Microglia are an essential component of the neuroprotective scar that forms after spinal cord injury. *Nat Commun*. 2019;10(1):518.
99. Rivest S. Regulation of innate immune responses in the brain. *Nat Rev Immunol*. 2009;9(6):429-39.
100. Adams KL, Gallo V. The diversity and disparity of the glial scar. *Nat Neurosci*. 2018;21(1):9-15.
101. Celano CM, Daunis DJ, Lokko HN, Campbell KA, Huffman JC. Anxiety Disorders and Cardiovascular Disease. *Curr Psychiatry Rep*. 2016;18(11):101.

Tables

Table 1: Summary of microglial morphometric parameters of sham and HF rats for the PVN and CeA

Table shows individual values (mean \pm SEM) of all analyzed microglial parameters, N = number of analyzed microglia, n= number of animals per group, CeA = central amygdala, PVN = paraventricular nucleus, S1BF = somatosensory cortex barrel field 1.

Brain region	Group	Cell volume (μm^3)	Surface area (μm^2)	Filament length (μm)	Dendritic branches	Dendritic segments	Filament terminals	IBA1 intensity (AU)
PVN	Sham 8w N=381 n=4	3157 \pm 112	4048 \pm 99	745 \pm 21	104 \pm 3	219 \pm 7	116 \pm 4	9449 \pm 123
	Sham 14w N=365 n=4	3098 \pm 119	4100 \pm 107	736 \pm 18	102 \pm 4	224 \pm 8	118 \pm 6	9385 \pm 135
	Sham 16w N=389 n=4	3181 \pm 122	4068 \pm 81	761 \pm 25	100 \pm 5	216 \pm 7	117 \pm 6	9522 \pm 139
	HF 8w N=378 n=4	2838 \pm 58	3868 \pm 75	642 \pm 12	82 \pm 2	171 \pm 5	90 \pm 3	11138 \pm 118
	HF 14w N=407 n=4	2212 \pm 74	3424 \pm 64	629 \pm 35	78 \pm 2	163 \pm 7	85 \pm 3	12764 \pm 202
	HF 16w N=399 n=4	2012 \pm 69	3233 \pm 59	524 \pm 39	72 \pm 3	150 \pm 5	83 \pm 4	12783 \pm 231
CeA	Sham 8w N=377 n=4	3588 \pm 137	4885 \pm 119	841 \pm 28	109 \pm 6	219 \pm 7	114 \pm 3	10134 \pm 137
	Sham 14w N=339 n=4	3644 \pm 122	4966 \pm 131	865 \pm 31	102 \pm 2	214 \pm 5	116 \pm 4	10073 \pm 144
	Sham 16w N=354 n=4	3691 \pm 123	4904 \pm 127	833 \pm 24	104 \pm 5	216 \pm 7	114 \pm 3	10285 \pm 180
	HF 8w N=363 n=4	3634 \pm 119	4700 \pm 124	765 \pm 29	106 \pm 4	222 \pm 7	112 \pm 3	10344 \pm 176
	HF 14w N=355 n=4	4418 \pm 187	4964 \pm 144	781 \pm 28	92 \pm 4	192 \pm 8	100 \pm 3	11314 \pm 277
	HF 16w N=332 n=4	3180 \pm 115	4395 \pm 163	623 \pm 24	89 \pm 3	179 \pm 6	94 \pm 4	12779 \pm 357
S1BF	Sham 14w N=139 n=4	4577 \pm 138	6008 \pm 234	967 \pm 31	125 \pm 5	261 \pm 8	135 \pm 7	10539 \pm 183
	HF 14w N=162 n=4	4257 \pm 130	5664 \pm 224	957 \pm 31	126 \pm 4	264 \pm 8	138 \pm 8	10647 \pm 171

Figures

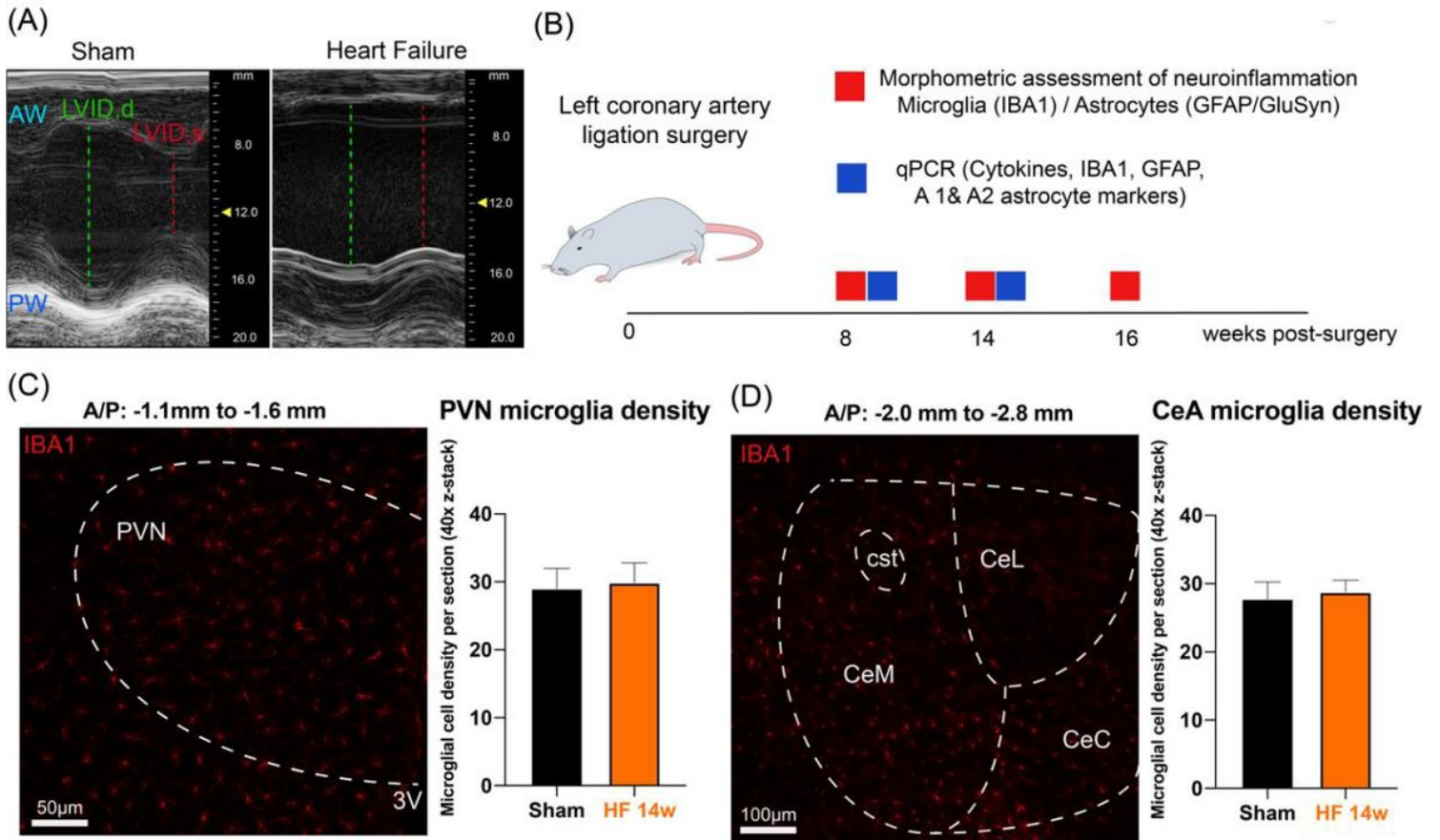


Figure 1

Heart failure does not alter microglial cell density in the PVN or CeA (a) Representative image showing the echocardiographic assessment left ventricular cardiac function in a sham and HF rats. (b) timetable depicting morphometric assessments and qPCR at 8-, 14- and 16- weeks post-surgery, (c, d) Representative confocal images showing IBA1-labeled microglia (red) in the PVN and CeA. Bar graphs show quantification of microglial density within the PVN and CeA in sham and HF rats 14 weeks post-surgery. 3V: third ventricle, AW: anterior wall, CeC: central amygdala capsular division, CeL: central amygdala lateral division, CeM: central amygdala medial division, cst: commissural stria terminalis, LVID, d and LVID, s: left ventricle internal dimensions in diastole and systole, PVN: paraventricular nucleus, PW: posterior wall.

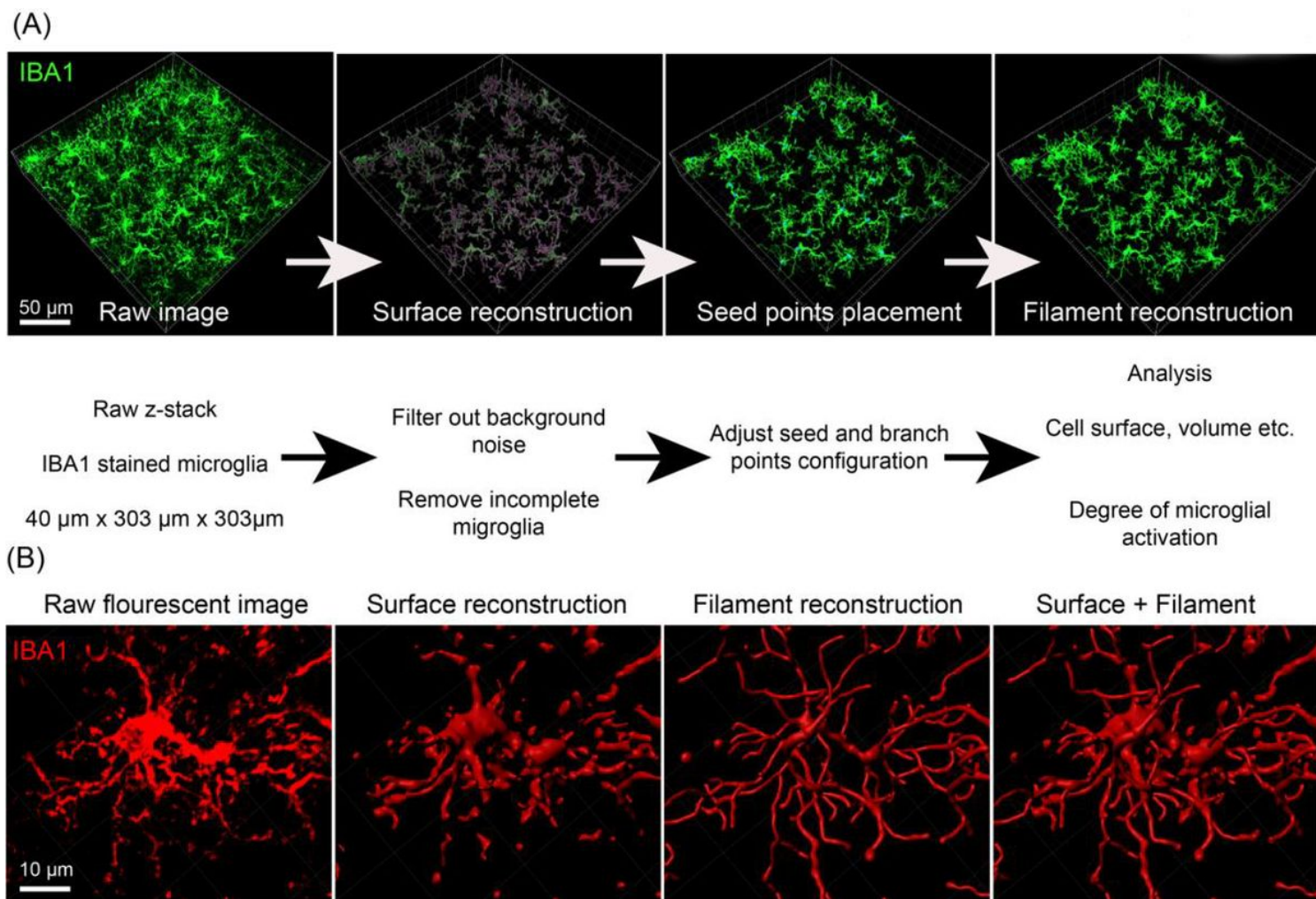


Figure 2

Three-dimensional reconstruction of microglia surface and filaments using IMARIS (a) schematic depiction of the sequential steps used for the 3D morphometric reconstruction and assessment of microglia (IBA1, green), (b) confocal images show the step-by-step process for three-dimensional reconstruction of a single microglia (IBA1, red). For image processing, colors were changed from red to green in IMARIS for better visibility and increased precision during manual editing of reconstructed microglia. Note the merging of red (raw fluorescence) and green (surface reconstruction) channels in the top panel.

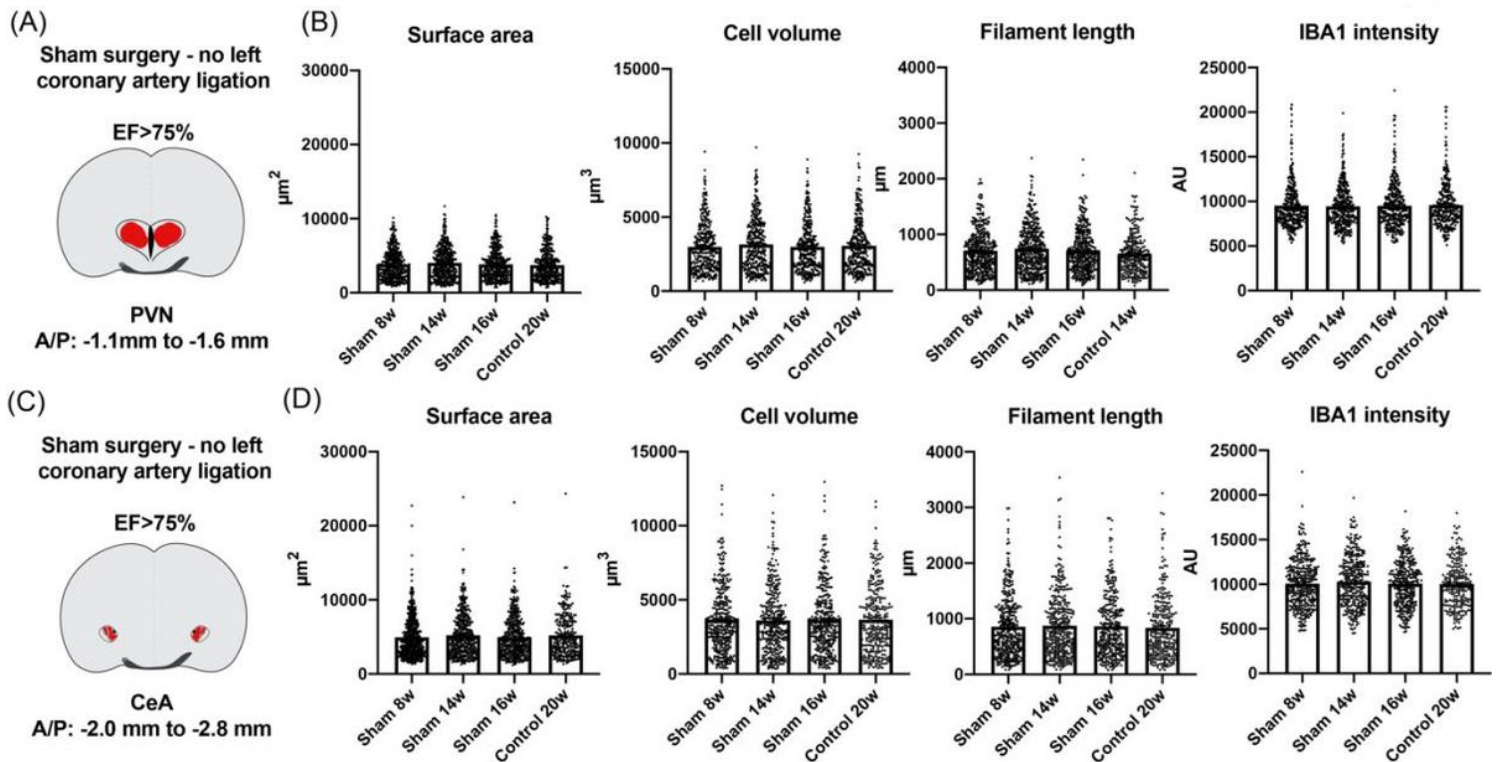


Figure 3

Sham surgery per se does not alter the morphology of PVN or CeA microglia (a) brain scheme shows the topographic location of PVN microglia that have been used for the morphometric assessment. The red area within the PVN (heart-shaped nucleus) highlights the fraction of the nucleus where pictures were taken, (b) dot-plot graphs show the individual values of PVN microglia for surface area, cell volume, filament length and IBA 1 intensity for the non-surgery control (N=357 from 4 rats), and sham rats at 8, 14 and 16 weeks post-surgery (n=381 from 4 rats, n= 365 from 4 rats and n=389 from 4 rats, respectively), (c) brain scheme shows the topographic location of CeA microglia that have been used for the morphometric assessment. The red area within the CeA highlights the divisions where pictures were taken, (d) dot-plot graphs show the individual values of CeA microglia for surface area, cell volume, filament length and IBA 1 intensity for the non-surgery control (N=297 from 4 rats), and sham rats at 8, 14 and 16 weeks post-surgery (N=377 from 4 rats, N=339 from 4 rats and N=354 from 4 rats, respectively).

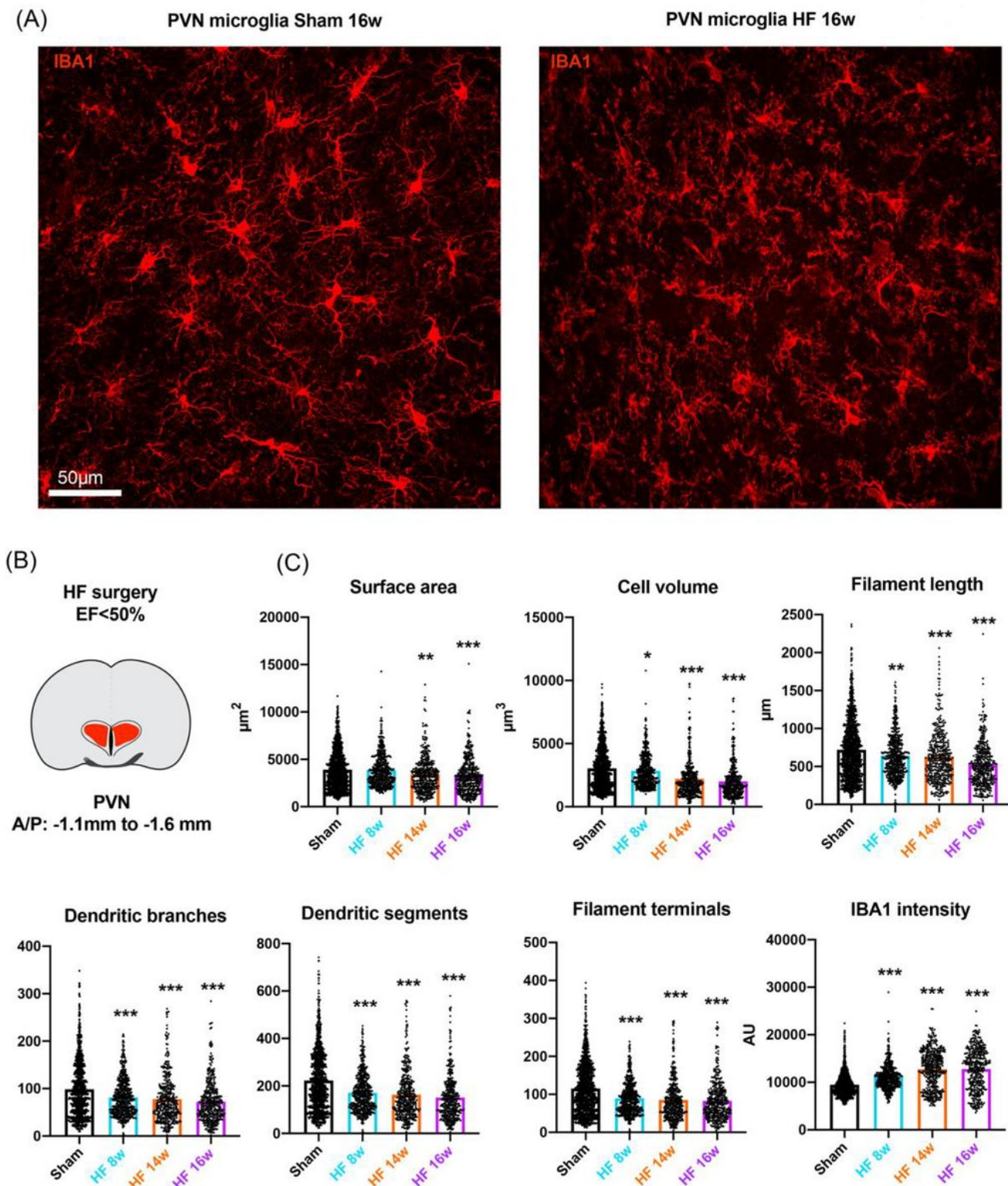


Figure 4

HF-induced morphometric changes in PVN microglia (a) representative confocal images show IBA1-stained microglia in the PVN of HF and sham rats 16 weeks post-surgery, (b) brain scheme shows the topographic location of PVN microglia that have been used for the morphometric assessment. The red area within the PVN (heart-shaped nucleus) highlights the fraction of the nucleus where pictures were taken, (c) dot-plot graphs show the individual values of PVN microglia for surface area, cell volume,

filament length, dendritic branches, dendritic segments, filament terminals and IBA 1 intensity for sham rats (N=1135 from 12 rats, pooled) and HF rats at 8, 14 and 16 weeks post-surgery (N=378 from 4 rats, N=407 from 4 rats and N=399 from 4 rats, respectively). * $p < 0.05$, ** $p < 0.01$ and *** $p < 0.0001$ vs. respective sham, one-way ANOVA followed by Tukey post-hoc test.

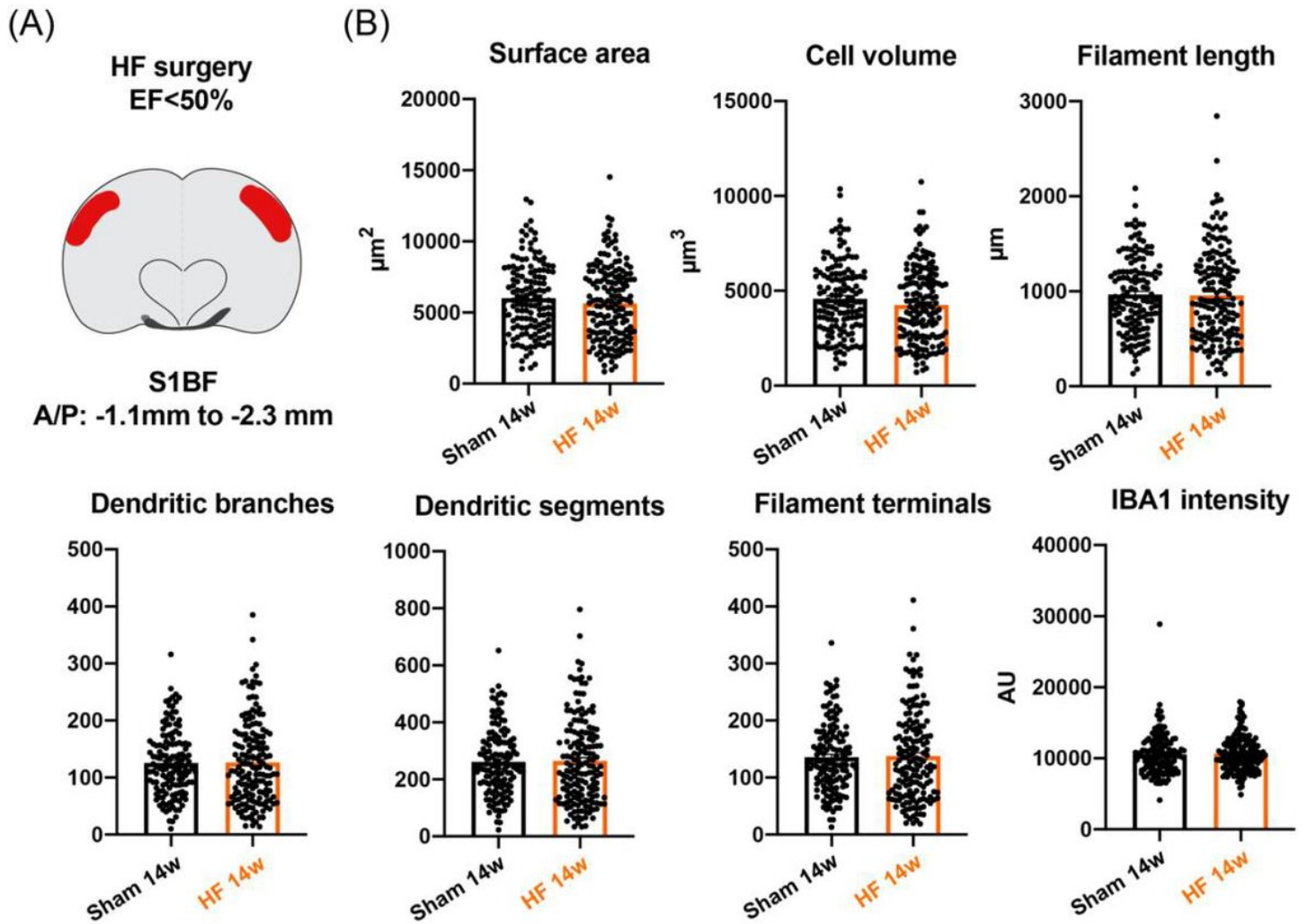


Figure 5

HF does not induce morphometric changes in somatosensory cortex 1 barrel field microglia (a) brain scheme shows the topographic location of S1BF microglia that have been used for the morphometric assessment. The red area highlights the S1BF, (b) dot-plot graphs show the individual values of S1BF microglia for surface area, cell volume, filament length, dendritic branches, dendritic segments, filament terminals and IBA 1 intensity for sham rats (n=4) and HF rats (n= 4).

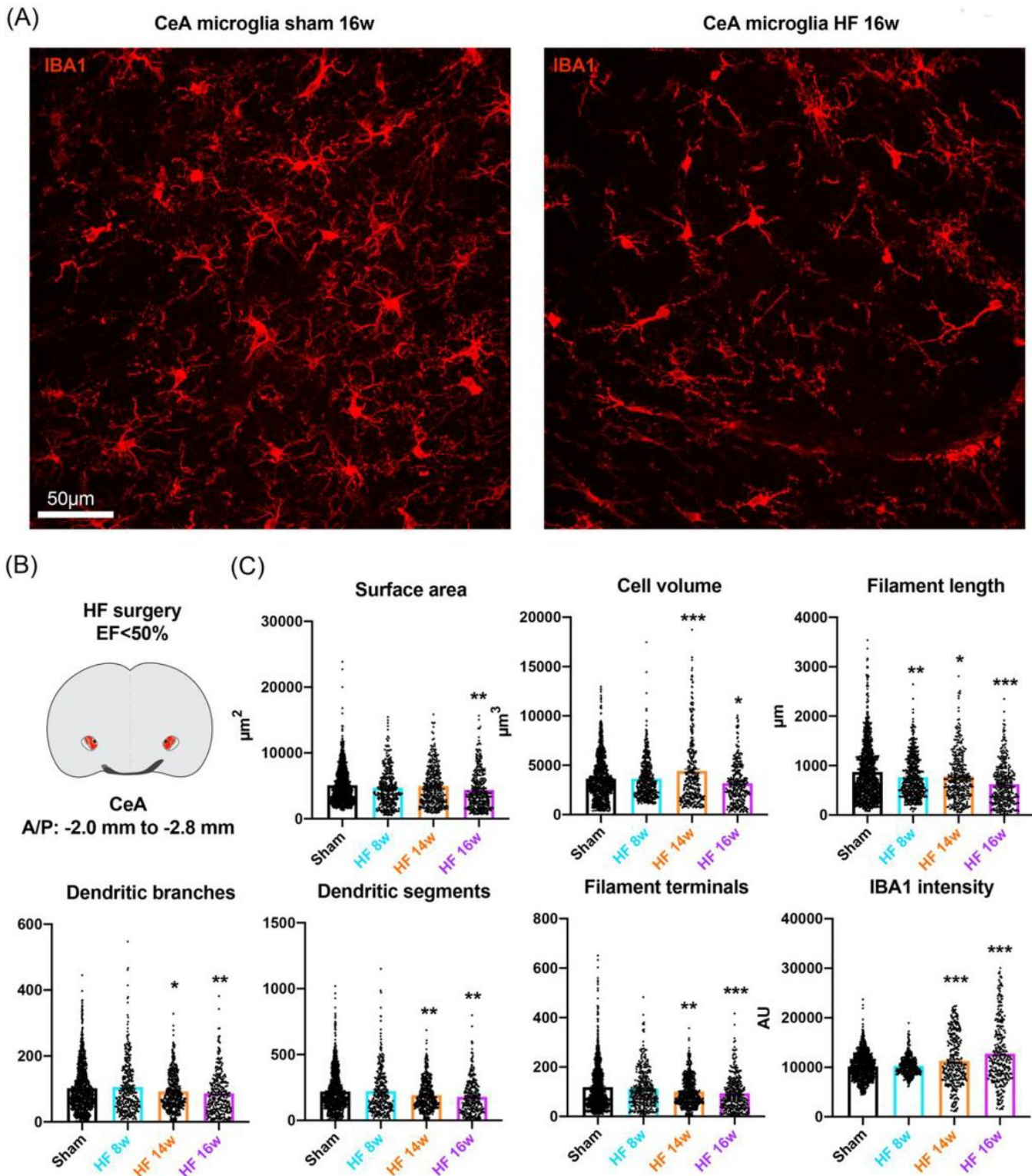


Figure 6

HF-induced morphometric changes in CeA microglia (a) representative confocal images show IBA1-stained microglia in the PVN of HF and sham rats 16 weeks post-surgery, (b) brain scheme shows the topographic location of CeA microglia that have been used for the morphometric assessment. The red dotted line highlights the CeA, (c) dot-plot graphs show the individual values of CeA microglia for surface area, cell volume, filament length, dendritic branches, dendritic segments, filament terminals and IBA 1

intensity for sham rats (N=1070 from 12 rats, pooled) and HF rats at 8, 14 and 16 weeks post-surgery (N=363 from 4 rats, N=355 from 4 rats and N= 332 from 4 rats, respectively). * $p < 0.05$, ** $p < 0.01$ and *** $p < 0.0001$ vs respective sham, one-way ANOVA followed by Tukey post-hoc test.

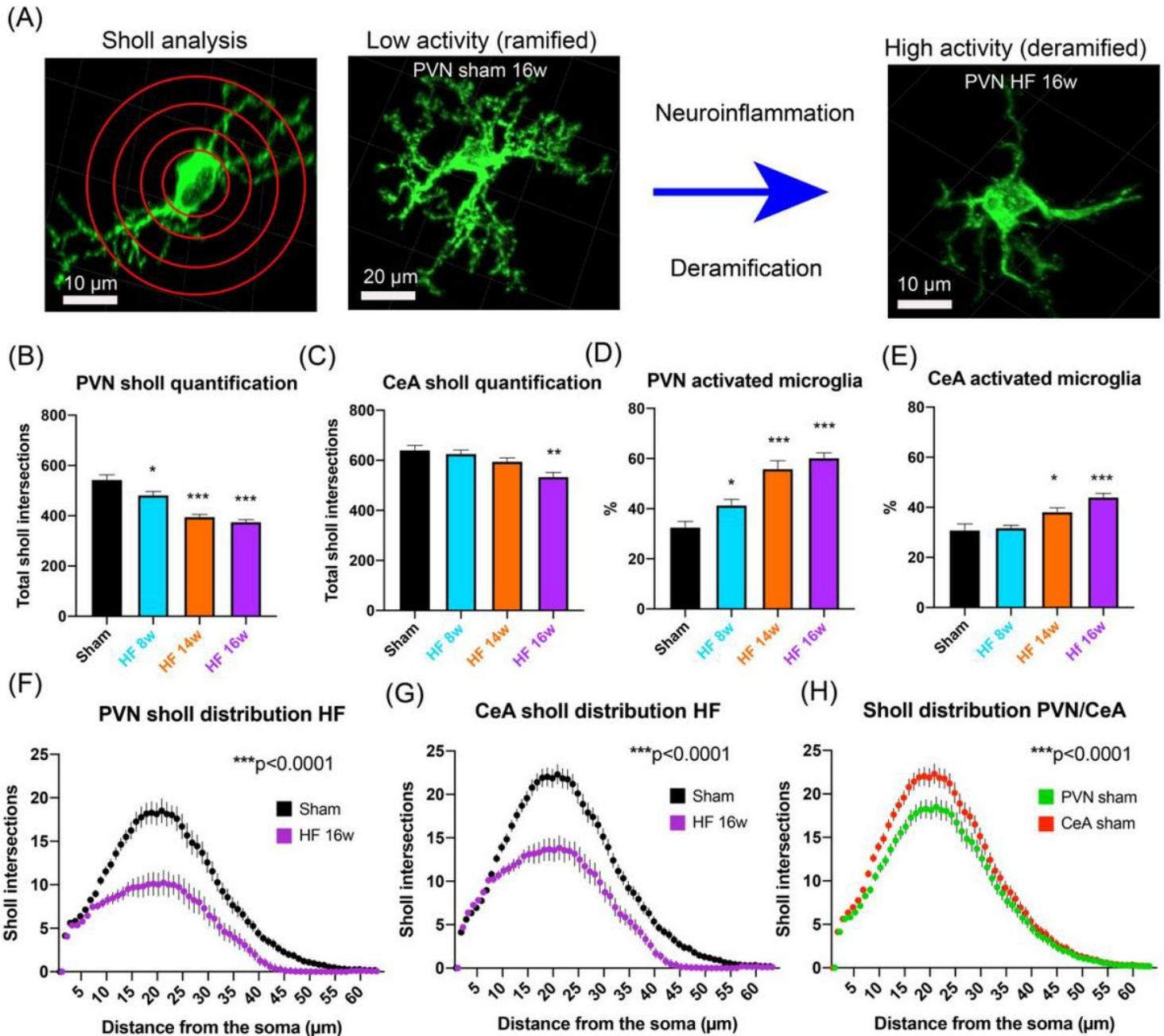


Figure 7

HF induced deramification and increased the proportion of activated microglia in the PVN and CeA (a) scheme depicts the HF-induced transition from low activity (ramified) to high activity (deramified) microglia. Red circles depict superimposed spheres centered around microglia somata used for Sholl analysis, (b, c) bar graphs show the mean number of total of Sholl intersections for PVN and CeA microglia in sham rats (n=12, pooled) and HF rats at 8, 14 and 16 weeks post-surgery (n=4/group), (d, e) bar graphs show the mean proportion of activated microglia in the PVN and CeA in sham rats (n=12, pooled) and HF rats at 8, 14 and 16 weeks post-surgery (n=4/group), (f-g) mean distribution plots of the

number of Sholl intersections as a function of the distance from the microglial soma for sham and HF rats 16 weeks post-surgery (n=4/group), (h) distribution plot comparing Sholl intersections as a function of the distance from the microglial soma for PVN and CeA microglia (n=12/group, pooled). *p<0.05, **p<0.01 and ***p<0.0001 vs. respective sham, two-way ANOVA or one-way ANOVA followed by Tukey post-hoc test.

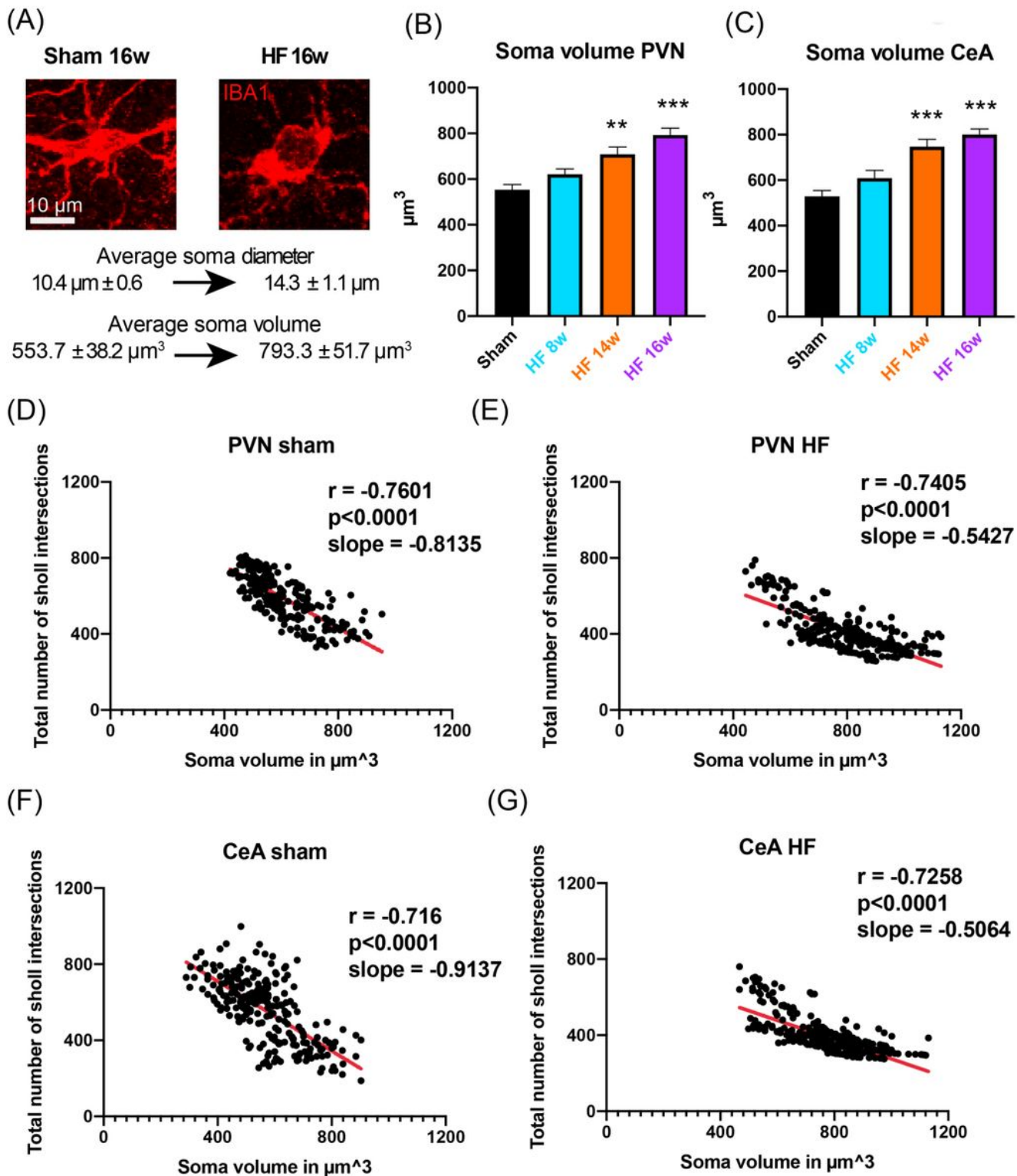


Figure 8

HF-induced somatic swelling of PVN and CeA microglia is correlated with microglial deramification (a) confocal images show a representative example of HF-induced microglial swelling, (b, c) bar graphs show the mean microglia somata volume in the PVN and CeA in sham rats (n=12, pooled) and HF rats at 8, 14 and 16 weeks post-surgery (n=4/group), (d-g) plots showing the total number of Sholl intersections as a function of soma volume for individual microglial cells in the PVN of sham (d) and HF (e) rats and in the CeA of sham (f) and HF (g) rats. Red lines represent best-fit lines assuming a non-linear relationship between the total number of Sholl intersections and soma volume. **p<0.01 and ***p<0.0001 vs respective sham, one-way ANOVA followed by Tukey post-hoc test or Pearson correlation.

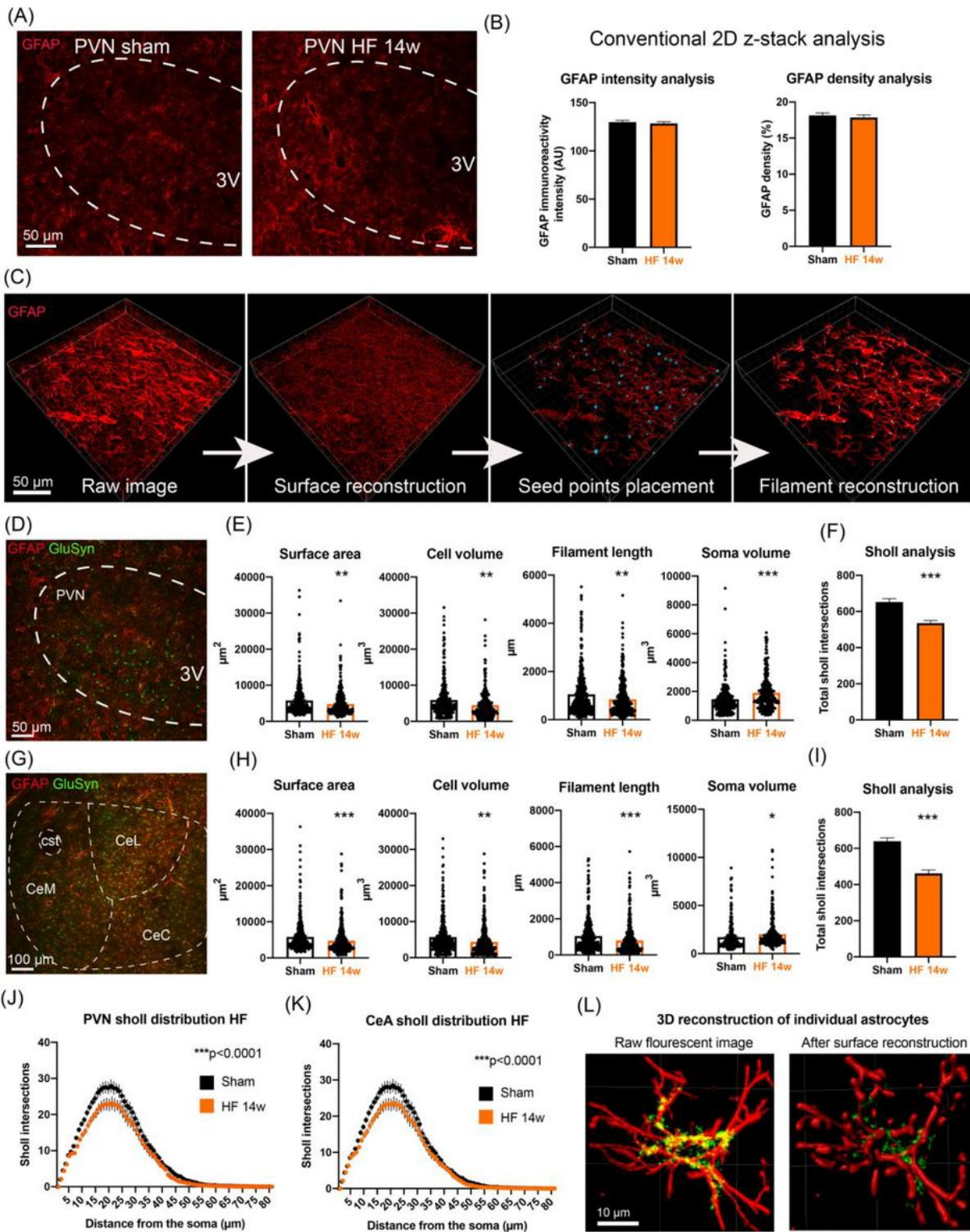


Figure 9

HF-induced morphometric changes in PVN and CeA astrocytes (a) representative confocal images show GFAP-labeled (red) PVN astrocytes in sham and HF rats, (b) bar graphs depict the mean GFAP immunoreactivity intensity (left panel) and density (right panel) obtained from a 2D z-stack analysis (Methods) in sham (n=12, pooled) and HF rats (n=4), (c) schematic depiction of sequential steps used for the 3D morphometric reconstruction and assessment of astrocytic processes using IMARIS (GFAP, red),

(d) representative confocal image showing PVN astrocytes in a sham rat stained with GFAP (red) and GluSyn (green), (e) dot-plot graphs show the individual values of PVN microglia for surface area, cell volume, filament length and IBA1 intensity in sham (n=4) and HF rats 14 weeks post-surgery (n=4), (f) bar graph shows the mean number of total sholl intersections in PVN astrocytes in sham (n=4) and HF rats 14 weeks post-surgery (n=4), (g) representative confocal image showing CeA astrocytes stained with GFAP (red) and GluSyn (green) in a sham rat, (h) dot-plot graph show the individual values of CeA microglia for surface area, cell volume, filament length and IBA1 intensity in sham (n=4) and HF rats 14 weeks post-surgery (n=4) (i) bar graph shows the mean number of total Sholl intersections in CeA astrocytes in sham (n= 4) and HF rats 14 weeks post-surgery (n=4), (j, k) mean distribution plots of the number of Sholl intersections as a function of the distance from the microglial soma for sham and HF rats 14 weeks post-surgery (n=4/group), (l) confocal images show a single PVN astrocyte from a sham animal before and after surface reconstruction with IMARIS. * $p < 0.05$, ** $p < 0.01$ and *** $p < 0.0001$ vs. respective sham, Student's-t test or two-way ANOVA.

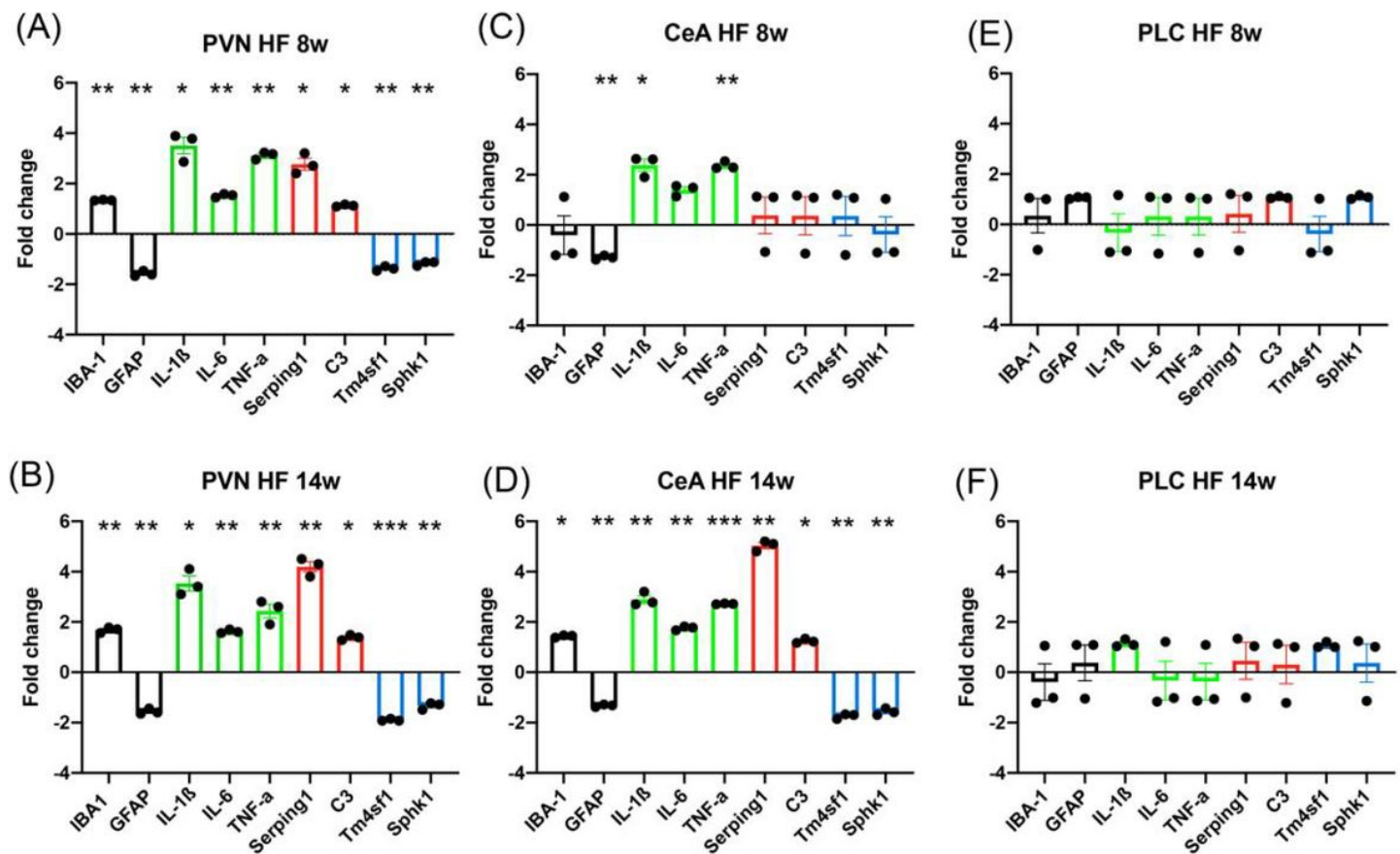


Figure 10

HF-induced changes in NI-associated microglia and astrocyte marker mRNA levels (a-f) bar graphs show the mean fold change in mRNA transcript levels in HF rats compared to sham rats in the PVN (a, b), the CeA (c, d) and the PLC (e, f). All graphs depict the fold changes of mRNA levels in HF group compared to their respective shams. Green bars: cytokines, red bars: a1 astrocyte markers, blue bars: a2 astrocyte

markers. * $p < 0.05$, ** $p < 0.01$ and *** $p < 0.0001$ vs. respective controls, one sample t-test, theoretical mean=1.